Nanoscale

ROYAL SOCIETY OF CHEMISTRY

REVIEW

View Article Online
View Journal | View Issue

Cite this: *Nanoscale*, 2023, **15**, 8508

Wet-chemistry synthesis of two-dimensional Pt- and Pd-based intermetallic electrocatalysts for fuel cells

Jingchun Guo,*[a] Wei Liu,[a] Xucheng Fu *[a] and Shilong Jiao *[b]

Two-dimensional (2D) noble-metal-based nanomaterials have attracted tremendous attention and have widespread promising applications as a result of their unique physical, chemical, and electronic properties. Especially, 2D Pt- and Pd-based intermetallic nanoplates (IMNPs) and nanosheets (IMNSs) are widely studied for fuel cell (FC)-related reactions, including the cathodic oxygen reduction reaction (ORR) and anodic formic acid, methanol and ethanol oxidation reactions (FAOR, MOR and EOR). Wet-chemistry synthesis is a powerful strategy to prepare metallic nanocrystals with well-controlled dispersity, size, and composition. In this review, a fundamental understanding of the FC-related reactions is firstly elaborated. Subsequently, the current wet-chemistry synthesis pathways for 2D Pt- and Pd-based IMNPs and IMNSs are briefly summarized, as well as their electrocatalytic applications including in the ORR, FAOR, MOR, and EOR. Finally, we provide an overview of the opportunities and current challenges and give our perspectives on the development of high-performance 2D Pt- and Pd-based intermetallic electrocatalysts towards FCs. We hope this review offers timely information on the synthesis of 2D Pt- and Pd-based IMNPs and IMNSs and provides guidance for the efficient synthesis and application of them.

Received 28th February 2023,
Accepted 11th April 2023

DOI: 10.1039/d3nr00955f

rsc.li/nanoscale

1. Introduction

The ever-increasing energy demand and excessive consumption of traditional fossil fuels result in an energy crisis and numerous environmental problems including air pollution and global warming.[1–3] Environment-friendly, clean, efficient, reliable, and sustainable energy technologies such as solar cells,[4,5] Li-ion batteries,[6,7] and fuel cells (FCs)[8,9] are urgently required to replace fossil fuels. FCs can convert chemically stored energy into electrical energy by the anodic electrooxida-

[a]*Department of Experimental and Practical Teaching Management, West Anhui University, Lu'an 237012, China. E-mail: 43000013@wxc.edu.cn, fxc8307@wxc.edu.cn*
[b]*School of Materials, Key Lab for Special Functional Materials of Ministry of Education, Henan University, Jinming Avenue, Kaifeng 475001, China. E-mail: sljiao@henu.edu.cn*

Jingchun Guo

Jingchun Guo is now working at West Anhui University. He received his bachelor's degree from Jilin University in 2010 and his Ph.D. degree from Hokkaido University in 2017. After graduation, he joined Shenzhen University as a postdoctoral fellow in 2018. His research interests include the controllable synthesis of metallic nanocrystals related to fuel cells and electrochemical catalysis.

Wei Liu

Wei Liu is now working at West Anhui University. He received his bachelor's degree from Anhui Normal University in 2011 and his Ph.D. degree from Dalian University of Technology in 2017. After graduation, he joined Xi'an Jiaotong University as a postdoctoral fellow in 2017. His research interests include the fundamental study of low temperature plasma sources, ion beams and material surface processing.

tion of chemical fuels (hydrogen, formic acid, methanol, and ethanol, *etc*.) and the cathodic oxygen reduction reaction (ORR).[8,9] FCs are considered potential candidates to replace conventional energy conversion devices (for example, internal combustion engines) fed with fossil fuels to supply energy in the future due to their high-energy conversion efficiency and relatively low working temperatures.[10,11] For example, proton exchange membrane FCs (PEMFCs) refueled with hydrogen produce water as a byproduct, making them one of the most promising solutions because of zero emission. However, the difficulty in O_2 activation and cleavage of strong O–O bonds involves four coupled proton and electron transfers, which causes sluggish kinetics of the ORR, thus limiting the commercialization of FCs. The Pt nanocatalyst shows the best electrocatalytic ORR performance among individual metals.[12] Therefore, carbon-supported Pt-based nanocatalysts have been utilized as commercial electrocatalysts in applied FCs.[13] Unfortunately, the low content, limited activity and poor durability of Pt put pressure on the cost and development of FCs.[14,15]

Several works demonstrated that alloying Pt with other metals could empower the alloyed catalysts with improved performance.[8–10] For example, it was reported that Pt_3Co, Pt_3Fe, and Pt_3Ni exhibited much higher ORR activity than that of pure Pt and other Pt-based alloys.[10] As a result, multimetallic alloys with various sizes and morphologies have been created by researchers to boost the activity and durability of the cathodic ORR.[12–14] Two types of materials with disordered and ordered crystal structures will be formed by two or more metal elements, which are called intermetallic nanocrystals (NCs) and random alloys, respectively.[16–19] The random alloys are a simple mixture and random distribution of several metal elements without elemental ordering, in which the elemental crystal structure is predominated by one of the constituent elements. However, the intermetallic NCs are compounds with a defined stoichiometry, and well-controlled crystal structure arising from long-range atomic ordering. As a result, the intermetallic NCs exhibit various advantages when applied as electrocatalysts due to the ordered atomic arrangement and more thermodynamically stable state compared to their random alloy counterparts even with the same chemical composition.[17–19] For example, it was demonstrated that CuPt intermetallic NCs with an ordered lattice showed significantly less leaching of Cu than their disordered CuPt random alloy counterparts with identical composition when electrochemically cycled in Ar-saturated 0.1 M $HClO_4$ solution.[20] It was reported that the ordered face-centered tetragonal (*fct*) PtFe intermetallic NCs had a lower oxygen adsorption energy and thus enhanced ORR activity compared to disordered face-centered cubic (*fcc*) PtFe NCs and Pt/C.[21] In addition, the regular structure of intermetallic NCs would ensure the homogeneity of the active sites, making intermetallic NCs ideal platforms for studying the structure-to-property relationships.[22] Therefore, intermetallic NCs are good candidates for promoting the kinetics of the ORR.

Exposing more catalytic active sites is also very important to improve the electrocatalytic performance of nanocatalysts. Therefore, unique nanostructures with a high active surface area including one-dimensional (1D) nanowires (NWs),[23–26] two-dimensional (2D) nanoplates (NPs) or nanosheets (NSs),[27–31] and three-dimensional (3D) nanoframes (NFs)[32–36] to expose more active adsorption sites for reactants and intermediate species have been proposed and successfully synthesized. Among these, 2D NPs or NSs with atomic thickness have attracted considerable attention due to their specific advantages of large lateral size, high electron mobility, high surface-to-volume ratio, and high density of unsaturated atoms when applied as electrocatalysts.[27] For example, Guo and coworkers successfully synthesized suprathin 2D 0.88 nm-thick (about four atomic layers) free-standing PdMo bimetallene.[37] The PdMo bimetallene/C achieved an extremely high ORR activity and excellent durability in alkaline solution owing to the large lateral size of the 2D nanostructure with a highly curved geometry (strain effect), multiple anchoring points between the bimetallene and the carbon support, and electronic interaction between palladium and molybdenum (alloying effect). In addition, the lattice of 2D NPs or NSs and the interface between the 2D cover and other active components provide meaningful confining environments for active sites, which has stimulated a new area of "confinement catalysis

Xucheng Fu

Xucheng Fu is now working at West Anhui University. He received his bachelor's degree from Anhui Normal University in 2000 and his Ph.D. degree from Hefei Institutes of Physical Science, Chinese Academy of Sciences, in 2011. His research interests include functional nanomaterials and photoelectrochemical analysis.

Shilong Jiao

Shilong Jiao received his Ph.D. degree in materials science from Shandong University. He is currently an assistant professor at Henan University. His current research interests include the preparation and characterization of nanocatalysts with various defects and the relationship between structural imperfections and the electrocatalytic performance of renewable energy-related reactions.

with 2D materials".[38] Deng and co-workers summarized 2D confinement catalysts with superior catalytic activity and stability including 2D lattice-confined single atoms and 2D cover-confined metals.[38] The electronic state of catalytic sites can be easily manipulated to match the energy level of the substrates within a lattice- and interface-confined environment, which realizes the feasibility of tuning the catalytic activity. Therefore, 2D Pt- and Pd-based IMNPs and IMNSs have attracted increasing attention as potential substitutes for FC electrocatalysis by integrating multiple advantages of alloying effects, structural merits, and a stable intermetallic phase.[39–42]

Several articles have reviewed the synthesis, properties, and applications of 2D Pt- and Pd-based nanomaterials.[39–42] However, a comprehensive outline of the preparation of 2D Pt- and Pd-based IMNPs and IMNSs and their related applications in FCs is still lacking. In this review, we first provide a fundamental understanding of the ORR, formic acid oxidation reaction (FAOR), methanol oxidation reaction (MOR), and ethanol oxidation reaction (EOR). Then, we comprehensively summarize the preparation of 2D Pt- and Pd-based IMNPs and IMNSs by wet-chemistry syntheses including one-pot synthesis (or co-reduction method) and seed-mediated synthesis. After highlighting their electrocatalytic applications in FCs including for the ORR, FAOR, MOR, and EOR, we address the current challenges associated with the controllable synthesis of 2D Pt- and Pd-based IMNPs and IMNSs and conclude the article with future perspectives.

2. Overview of fuel cells

FCs can generate efficient electron transfer in the external circuit by the transport of charged ions through the electrolyte, and thus, achieve the direct conversion of chemical energy from the electrooxidation of fuels (hydrogen, methanol, ethanol, and formic acid, *etc*.) into electrical energy at the anode and the ORR at the cathode, respectively.

2.1 Cathode

The ORR is significantly important because it plays a crucial role in the effective operation of FCs. Typically, the cleavage of strong O–O bonds leads to a complicated multielectron reaction involving different reaction intermediates including a "direct" four-electron pathway to generate O_2 species (H_2O in acidic solutions or OH^- in alkaline solutions) and an "indirect" two-electron pathway to generate hydrogen peroxide (H_2O_2).[10] Unanimously, the "direct" four-electron pathway is the most efficient because the generation of H_2O_2 reduces energy-conversion efficiency. Generally, a large amount of Pt loading in the cathode is required to accelerate the sluggish kinetics of the ORR and the production yield of H_2O_2 is generally very low (the experimentally calculated number of transferred electrons is very close to 4 on the current state-of-the-art Pt and Pd-based electrocatalysts).[12]

2.2 Anode

Hydrogen is mostly used as an anodic fuel due to its high power density and zero-carbon emission.[10] In addition, the reaction kinetics of the hydrogen oxidation reaction (HOR) is much higher than the ORR.[8] As a result, a very small amount of Pt loading is enough for the HOR.[8] However, hydrogen FCs face issues of storage, transportation, refueling and safety.[43,44] Liquid fuels including formic acid, methanal, and ethanal are much easier to store, transport and refuel compared with hydrogen. Therefore, the direct formic acid FCs (DFAFCs),[45,46] direct methanol FCs (DMFCs),[47–52] and direct ethanol fuel cells (DEFCs)[53–56] are thought to be perfect candidates for sustainable energy conversion and storage devices for transportable electronic devices. Here we give a brief introduction to the FAOR, MOR, and EOR to have a better understanding of the fundamental electrochemistry. Two pathways, namely, direct dehydrogenation (1: $HCOOH \rightarrow CO_2 + H_2 + 2e^-$) and dehydration (2: $HCOOH \rightarrow CO + H_2O$), for the FAOR were proposed to date.[15] The direct dehydrogenation reaction is more desirable because the dehydration reaction can generate a large amount of poisonous CO, which is easily adsorbed at the active sites and inhibits the electrocatalytic activity of the electrocatalysts. The MOR includes the adsorption of methanol, dehydrogenation and oxidation of CO or other carbonaceous intermediates to CO_2 without breaking C–C bonds (1: $CH_3OH + H_2O \rightarrow CO_2 + 6H^+ + 6e^-$, and 2: $CH_3OH + 6OH^- \rightarrow CO_2 + 5H_2O + 6e^-$).[49] There are two reaction pathways for the MOR: the direct pathway (CO-free pathway) and the indirect pathway (CO pathway).[49] The direct pathway is favored because CO (indirect pathway) would poison the electrocatalysts and hinder the conversion efficiency. Typically, there are two parallel pathways for the EOR (breaking C–C bonds C1: $CH_3CH_2OH + 3H_2O \rightarrow 2CO_2 + 12H^+ + 12e^-$, and without breaking C–C bonds C2: $CH_3CH_2OH + H_2O \rightarrow CH_3COOH + 4H^+ + 4e^-$).[55] The C1 pathway is favoured but much slower than the C2 pathway because the C1 pathway involves breaking of the C–C bond. The electrochemical kinetics of the FAOR, MOR, and EOR are orders of magnitude slower than that of the HOR.[44] Especially for the EOR, which involves a complicated process with several steps, such as ethanol adsorption, C–C bond scission, dehydrogenation, electrooxidation of adsorbed intermediates (*e.g.* CO) and the formation of soluble species (*e.g.* acetaldehyde and acetic acid), the reaction rate and conversion efficiency are strongly reduced. Therefore, the rational design and development of advanced 2D Pt- and Pd-based IMNPs and IMNSs with a high specific surface area, abundant surface active sites, modulated electronic structure, and optimized adsorption energy are important for improving the electrocatalytic activity.

3. Synthesis strategies

2D Pt- and Pd-based IMNPs and IMNSs are commonly synthesized by wet-chemistry synthesis methods, including one-pot synthesis and seed-mediated synthesis in the liquid phase, as shown in Fig. 1. One-pot synthesis realizes the simul-

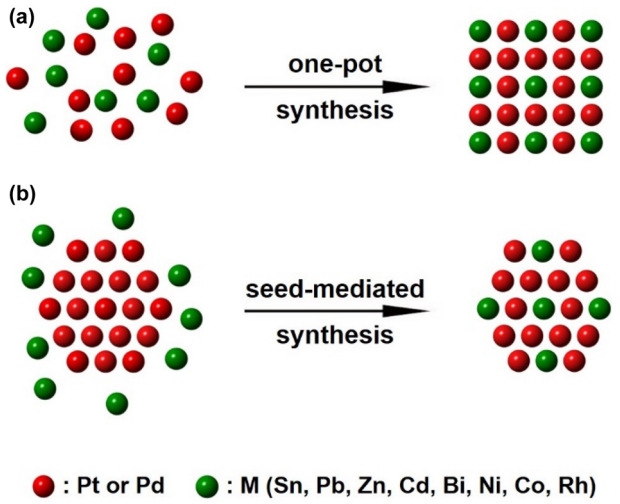

Fig. 1 Two typical synthesis strategies for 2D Pt- and Pd-based IMNPs and IMNSs. (a) One-pot synthesis. (b) Seed-mediated synthesis. Red spheres represent Pt or Pd elements, green spheres represent M (Sn, Pb, Zn, Cd, Bi, Ni, Co, Rh) elements.

taneous reduction of Pt (or Pd) and other metal-containing precursors (Sn, Pb, Zn, Cd, Bi, Rh, Co, Ni *etc.*) in one reactor with the help of reducing agents, surfactants, and other reactants, as depicted in Fig. 1a. In a typical seed-mediated synthesis, 2D Pd NPs or NSs utilized as seeds are synthesized firstly and additional metal ions are thermally reduced and diffuse into the seeds under mild reducing conditions in the liquid phase (Fig. 1b).

3.1. One-pot synthesis

3.1.1. 2D Pt-based intermetallic nanoplates

3.1.1.1 2D Pt–Bi intermetallic nanoplates. Guo *et al.* reported the use of 10 mg platinum(II) acetylacetonate ($Pt(acac)_2$), 9.6 mg bismuth(III) acetate ($Bi(Ac)_3$), 35.6 mg L-ascorbic acid (AA), and 50 mg NH_4Br in a mixture of 2.5 mL 1-octadecene (ODE) and 2.5 mL oleylamine (OAm) at 160 °C for 5 h to prepare 2D PtBi IMNPs with a thickness of 4.6 nm (Fig. 2a–d).[57] The transmission electron microscope (TEM) image in Fig. 2a shows that the majority of products are 2D NPs with either hexagonal or triangle shape. The high-resolution TEM (HRTEM) images in Fig. 2b and c demonstrate that the lattice spacings of the inner and edge regions are 0.35 nm (close to the (101) plane of hexagonal close-packed (*hcp*)-PtBi) and 0.22 nm (close to the (111) plane of *fcc*-Pt), respectively. Therefore, the 2D PtBi IMNPs are actually core/shell structures composed of an intermetallic *hcp*-PtBi core and an ultrathin *fcc*-Pt shell. The high-angle annular dark-field scanning TEM energy dispersive X-ray spectroscopy (HAADF-STEM-EDX) elemental mapping analysis in Fig. 2d demonstrates the homogeneous distribution of both Pt and Bi throughout the NPs. In addition, Huang *et al.* reported the use of 5 mg $Pt(acac)_2$, 7.6 mg $Bi(Ac)_3$, 50 mg phloroglucinol, and 150 mg polyvinylpyrrolidone (PVP) in 10 mL *N*,*N*-dimethylformamide (DMF) at 160 °C for 2 h under 1 bar CO to obtain 2D hexagonal PtBi IMNPs with a thickness of around 18 nm (Fig. 2e–g).[58] The HAADF-STEM image in Fig. 2e clearly shows the hexagonal morphology of the as-made PtBi IMNPs with a size of around 100 nm. The HRTEM image in Fig. 2f reveals the crystalline nature of the PtBi IMNPs with an interplanar spacing of 0.37 nm, which is assigned to the (100) plane of PtBi. The STEM-EDX elemental mapping analysis in Fig. 2g demonstrates the uniform distribution of Pt and Bi throughout the whole PtBi IMNP. Xie *et al.* successfully synthesized a series of heterogeneous *fcc*-Pt/*hcp*-PtBi thick-edge IMNPs ($Pt_{49}Bi_{51}$, $Pt_{64}Bi_{36}$, and $Pt_{85}Bi_{15}$) with a thickness of 3.1 nm, average size of around 41 nm, and tunable edge width (3.7, 6.0, 7.0 nm) by varying the input ratio of the Pt and Bi precursors (Pt : Bi = 3 : 4, 5 : 2, 5 : 1).[59] In addition, $Pt_{93}Bi_7$ nanoparticles that were not 2D NPs were obtained when the molar ratio of Pt and Bi precursors increased to 10 : 1. In a typical synthesis of $Pt_{87}Bi_{13}$ IMNPs, 10 mg (0.025 mmol) of $Pt(acac)_2$, 1.8 mg (0.005 mmol) of $BiCl_3{\cdot}3H_2O$, 35.6 mg of AA, and 50 mg of NH_4Br were added to a mixed solution of 2.5 mL OAm and 2.5 mL ODE at 160 °C for 5 h. The TEM image of $Pt_{87}Bi_{13}$ IMNPs in Fig. 2h illustrates high contrast between the edge and the center part, showing the feature of thin NPs and the surrounding thick edge. The HRTEM image of PtBi IMNPs in Fig. 2i shows clear lattice fringes of 0.19 nm on the thick edge, which is consistent with the interplanar distance of {200} planes of *fcc*-Pt. Furthermore, the lattice fringes with a spacing of 0.22 nm (Fig. 2j) in three directions with a cross angle of 60° correspond to the crystal plane spacing of {1210}, and the results indicate that the main facet of *hcp*-PtBi IMNPs is {0001}. The HAADF-STEM (Fig. 2h) and HAADF-STEM-EDX mapping images of a single PtBi IMNP (Fig. 2k) confirmed that Pt and Bi atoms were distributed over the whole NP and Pt enriched the edge area. The results indicate that the as-prepared PtBi IMNPs are heterojunction structures with intermetallic *hcp*-PtBi ultrathin NPs in the middle and *fcc*-Pt thick edges at the periphery. Sun *et al.* synthesized PtBi IMNPs with a thickness of 19.5 ± 2.8 nm and average edge length of 36.9 ± 4.9 nm using 8.0 mg $Pt(acac)_2$ (0.02 mmol), 7.7 mg $Bi(Ac)_3$ (0.02 mmol), and 250 mg PVP in 1.0 mL acetic acid glacial (HAc) and 8.0 mL DMF solution at 150 °C for 4 h.[60] The scanning electron microscopy (SEM) image in Fig. 2l shows the uniform hexagonal shape of PtBi IMNPs. The HRTEM image in Fig. 2m reveals that the lattice spacing is 0.37 nm, which is in agreement with the {100} lattice spacing of intermetallic PtBi. The HAADF-STEM image and the corresponding EDX elemental mappings in Fig. 2n manifest the homogeneous distribution of Pt and Bi elements.

3.1.1.2 2D Pt–Pb intermetallic nanoplates. Huang and coworkers reported the use of 10 mg $Pt(acac)_2$, 8 mg lead(II) acetylacetonate ($Pb(acac)_2$), and 35.6 mg AA in a mixture of 2.5 mL 1-ODE and 2.5 mL oleylamine (OAm) at 160 °C for 5 h to prepare 2D PtPb/Pt core/shell IMNPs that exhibit large biaxial strains with a thickness of 4.5 ± 0.6 nm and monodisperse edge length of 16 nm (Fig. 3a–c).[61] The TEM image in Fig. 3a shows the 2D hexagonal NP (HNP) morphology. The HRTEM image in Fig. 3b revealed different crystalline structures between the edge and interior of a single NP. The fast

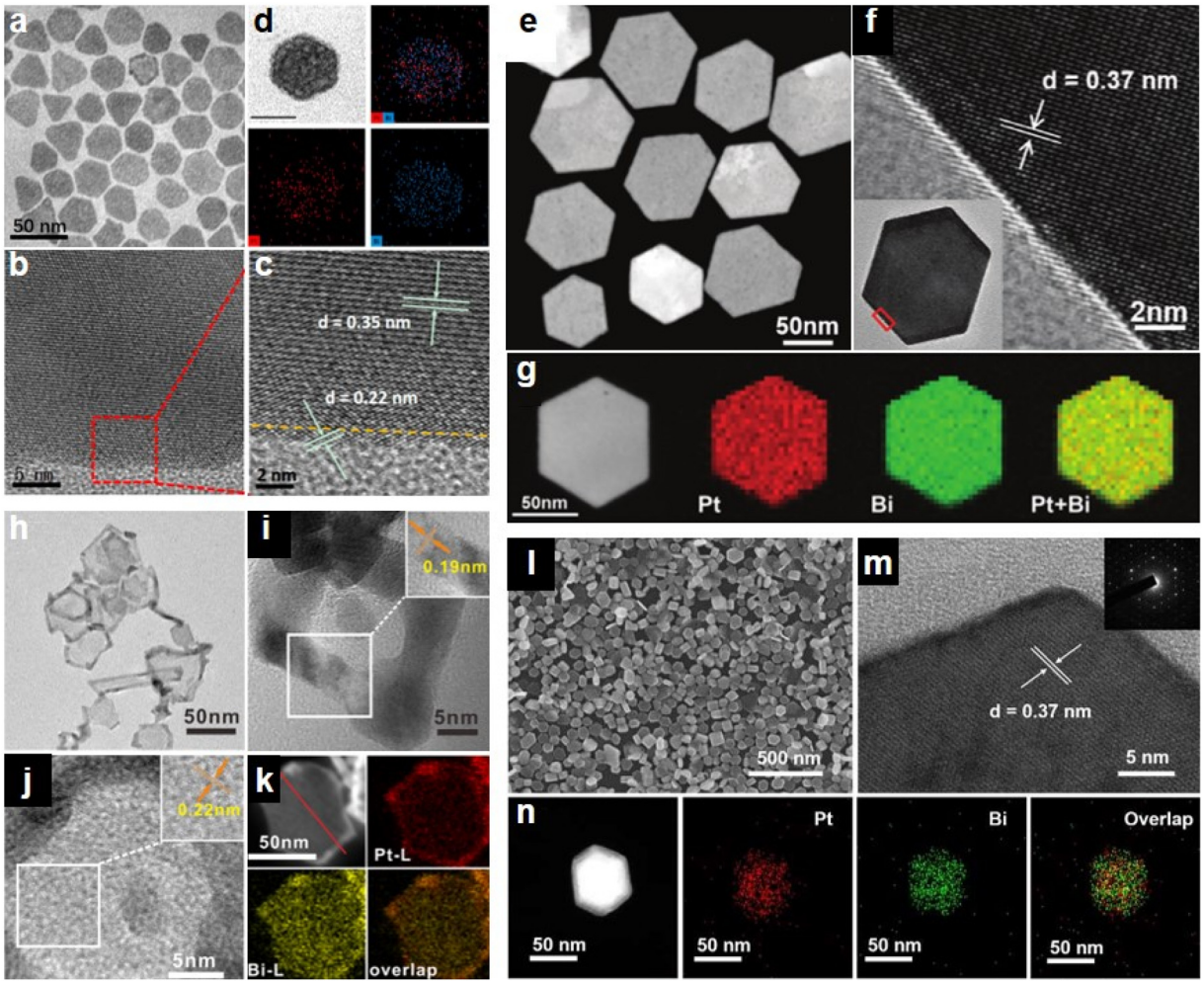

Fig. 2 (a) TEM, (b and c) HRTEM, and (d) STEM-EDX elemental mapping images of as-prepared PtBi/Pt core/shell IMNPs. This figure has been adapted from ref. 57 with permission from the American Chemical Society, copyright 2018. Representative (e) HAADF-STEM, (f) HRTEM, and (g) STEM-EDX elemental mapping images of PtBi IMNPs. This figure has been adapted from ref. 58 with permission from John Wiley and Sons, copyright 2020. (h) TEM image of heterogeneous *fcc*-Pt/*hcp*-PtBi thick-edge $Pt_{87}Bi_{13}$ IMNPs. HRTEM images of (i) the thick *fcc*-Pt edge, and (j) thin *hcp*-PtBi center. (k) HAADF-STEM and corresponding HAADF-STEM-EDX mapping images of a single *fcc*-Pt/*hcp*-PtBi thick-edge $Pt_{87}Bi_{13}$ IMNPs. This figure has been adapted from ref. 59 with permission from the American Chemical Society, copyright 2021. (l) SEM, (m) HRTEM, and (n) STEM-EDX element mapping images of hexagonal PtBi IMNPs. This figure has been adapted from ref. 60 with permission from John Wiley and Sons, copyright 2021.

Fourier transform (FFT) patterns indicate a cubic phase at the edge layer and a hexagonal phase of the interior (see the insets of Fig. 3b). The STEM-electron energy-loss spectroscopy (EELS) mapping of Pt and Pb distributions confirmed the presence of a Pt edge layer around the PtPb core. In addition, Guo *et al.* used the ion irradiation technique to control the defects and interfaces of 2D PtPb IMNPs.[62,63] The 2D PtPb IMNPs could be well transformed from single crystals into polycrystals with varying degrees of dislocations, subgrain boundaries, partial amorphization, crystalline/amorphous interfaces and a totally amorphous phase by controlling the C^+ or Kr^{3+} ion fluence.[62,63] Yao *et al.* injected 8 mL of DEG solution containing 10 mg $Pt(acac)_2$ and 40 mg $Pb(acac)_2$ into 12 mL DEG solution containing 1.554 g PVP maintained at 105 °C for 5 h under a nitrogen flow to obtain 2D PtPb IMNPs with a large surface area of the (102) facet.[64] As shown in Fig. 3d, 2D PtPb IMNPs with a hexagonal structure were successfully prepared with an average edge length of 36.6 nm. HRTEM images in Fig. 3e further show that the lattice spacing is 0.22 nm, which is indexed to the (102) facet of PtPb nanocrystals. EDX elemental mapping results in Fig. 3f show the uniform distributions of both Pt and Pb.

3.1.1.3 Polynary 2D Pt-based intermetallic nanoplates. Quan and co-workers obtained 2D PtSnBi IMNPs with controllable compositions including $Pt_{47}Sn_{16}Bi_{37}$, $Pt_{45}Sn_{25}Bi_{30}$, and $Pt_{45}Sn_{34}Bi_{21}$.[65] In a typical synthesis of 2D $Pt_{45}Sn_{25}Bi_{30}$ IMNPs, 20.5 mg $Pt(acac)_2$, 6.1 mg $SnCl_2$, 15 mg $Bi(AC)_3$, 350 mg cetyl trimethyl ammonium bromide (CTAB), and 80 mg AA were added to 5 mL OAm and 5 mL ODE at 220 °C for 1 h. The syntheses of $Pt_{47}Sn_{16}Bi_{37}$ and $Pt_{45}Sn_{34}Bi_{21}$ IMNPs were similar

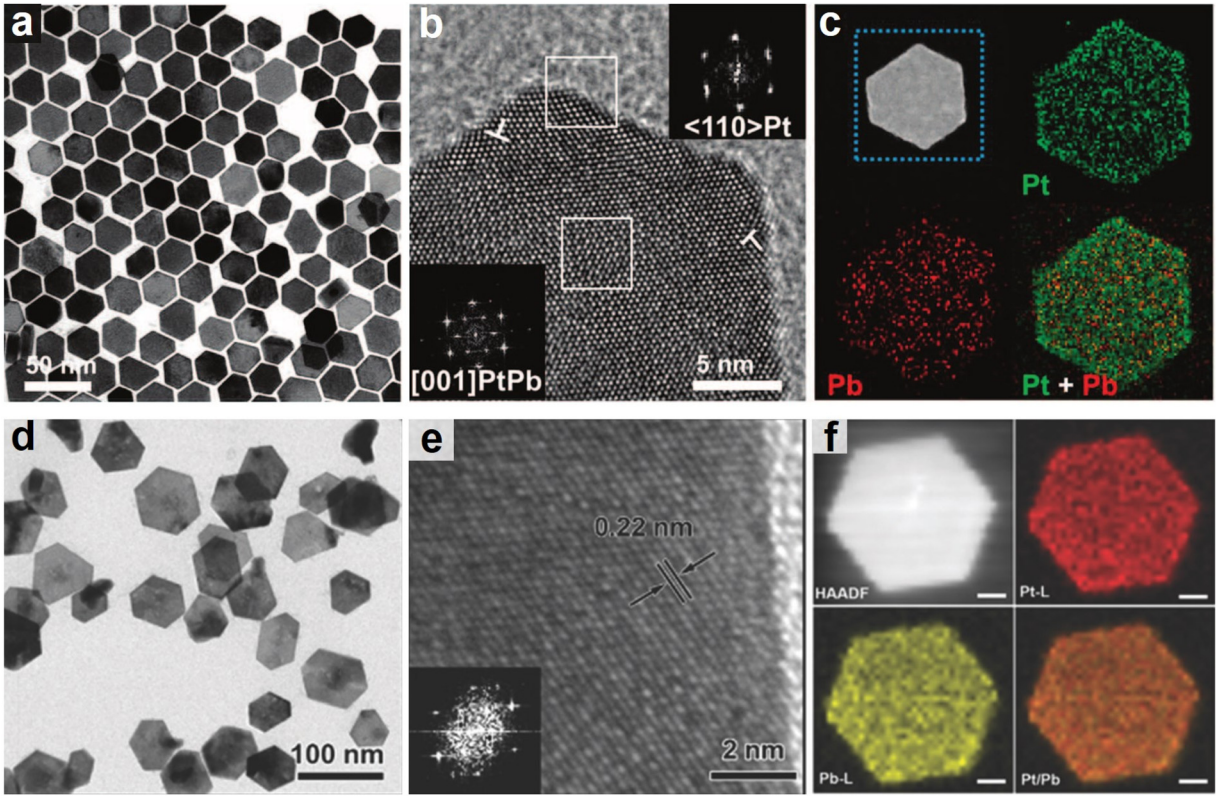

Fig. 3 (a) TEM and (b) HRTEM images and (c) STEM-EELS elemental mapping of 2D hexagonal PtPb/Pt core/shell IMNPs. Insets of Fig. 1b are the FFT patterns from the white squares at the edge of and inside the NPs, respectively. This figure has been adapted from ref. 61 with permission from the AAAS, copyright 2016. (d) TEM and (e) HRTEM images and (f) EDX mapping of 2D hexagonal PtPb IMNPs. All scale bars are 10 nm in (f). This figure has been adapted from ref. 64 with permission from the Royal Society of Chemistry, copyright 2020.

to that of the $Pt_{45}Sn_{25}Bi_{30}$ IMNPs except for the use of 8.5 mg $SnCl_2$ + 10 mg $Bi(AC)_3$ and 4 mg $SnCl_2$ + 17.5 mg $Bi(AC)_3$ as precursors, respectively. The TEM images in Fig. 4a reveal that the 2D PtSnBi IMNPs are well-dispersed with a typical hexagonal contour, accompanied by triangle, ribbon, and diamond shapes. The HAADF-STEM image in Fig. 4b shows the well-defined stacking sequences of bright and dark dots in a rhombic periodic arrangement throughout the whole NP. The average lattice spacing is found to be 0.366 nm, which is between that of the (100) plane of PtSn (0.355 nm) and PtBi (0.374 nm) intermetallic compounds. As shown in Fig. 4c, the atomic-resolution EDX mapping of a representative area demonstrates the atomic merging of Pt, Sn, and Bi elements. Additional analyses, as shown in Fig. 4d, verified that the fully ordered intermetallic NPs had Sn-terminated surfaces and isolated Pt atoms. Li *et al.* reported the synthesis of 2D intermetallic PtPbBi HNPs as new high-performance electrocatalysts.[66] In the typical synthesis of PtPbBi HNP-1, 20.50 mg of Pt $(acac)_2$, 9.95 mg of $Pb(acac)_2$, 18.88 mg of $Bi(NO_3)_3{\cdot}5H_2O$, 100 mg of AA, and 200 mg of CTAB were added to 5 mL OAm and 5 mL ODE at 210 °C for 30 min. PtPbBi HNP-2 and PtPbBi HNP-3 were synthesized by using 20.50 mg of $Pt(acac)_2$, 9.95 mg of $Pb(acac)_2$ and 16.52 mg of $Bi(NO_3)_3{\cdot}5H_2O$, and 20.50 mg of $Pt(acac)_2$, 9.95 mg of $Pb(acac)_2$ and 14.16 mg of $Bi(NO_3)_3{\cdot}5H_2O$, respectively. The TEM image in Fig. 4e reveals the hexagonal morphology. The particle size and thickness of the samples are around 16.7 nm and 6.8 nm. As shown in Fig. 4f, the HRTEM image clearly shows the hexagonal angularities, and the internal lattice spacing is found to be 0.234 nm, which is slightly larger than that of the Pt (111) crystalline plane and is attributed to the incorporation of Pb and Bi atoms. The corresponding FFT pattern in Fig. 4f indicated that the NPs exhibited an *hcp* phase. The EDX maps of the representative area in Fig. 4g show the uniform distribution of Pt, Pb, and Bi in the HNP. Quan and co-workers synthesized high-entropy 2D PtRhBiSnSb IMNPs by adding 20.4 mg $Pt(acac)_2$, 6.9 mg $Rh(acac)_3$, 17.5 mg $Bi(AC)_3$, 3.0 mg $SnCl_2$, 3.8 mg $SbCl_3$, 80 mg AA, and 350 mg CTAB to 5 mL OAm and 5 mL ODE at 220 °C for 1 h.[67] 2D PtBiSnSb IMNPs were also prepared by using 14.0 mg $Bi(AC)_3$ without adding $Rh(acac)_3$ under the same experimental conditions in high-entropy 2D PtRhBiSnSb IMNPs. The TEM images in Fig. 4h show well-dispersed HNPs with an average edge length of around 6.2 nm. Well-defined stacking sequences of atomic columns throughout the NPs, as shown in the HAADF-STEM image in Fig. 4i, reveal the ordered atomic arrangements in high-entropy 2D PtRhBiSnSb IMNPs. The lattice spacing of the (100) planes on the edge of the NPs is found to be 0.361 nm, which is located between that of the

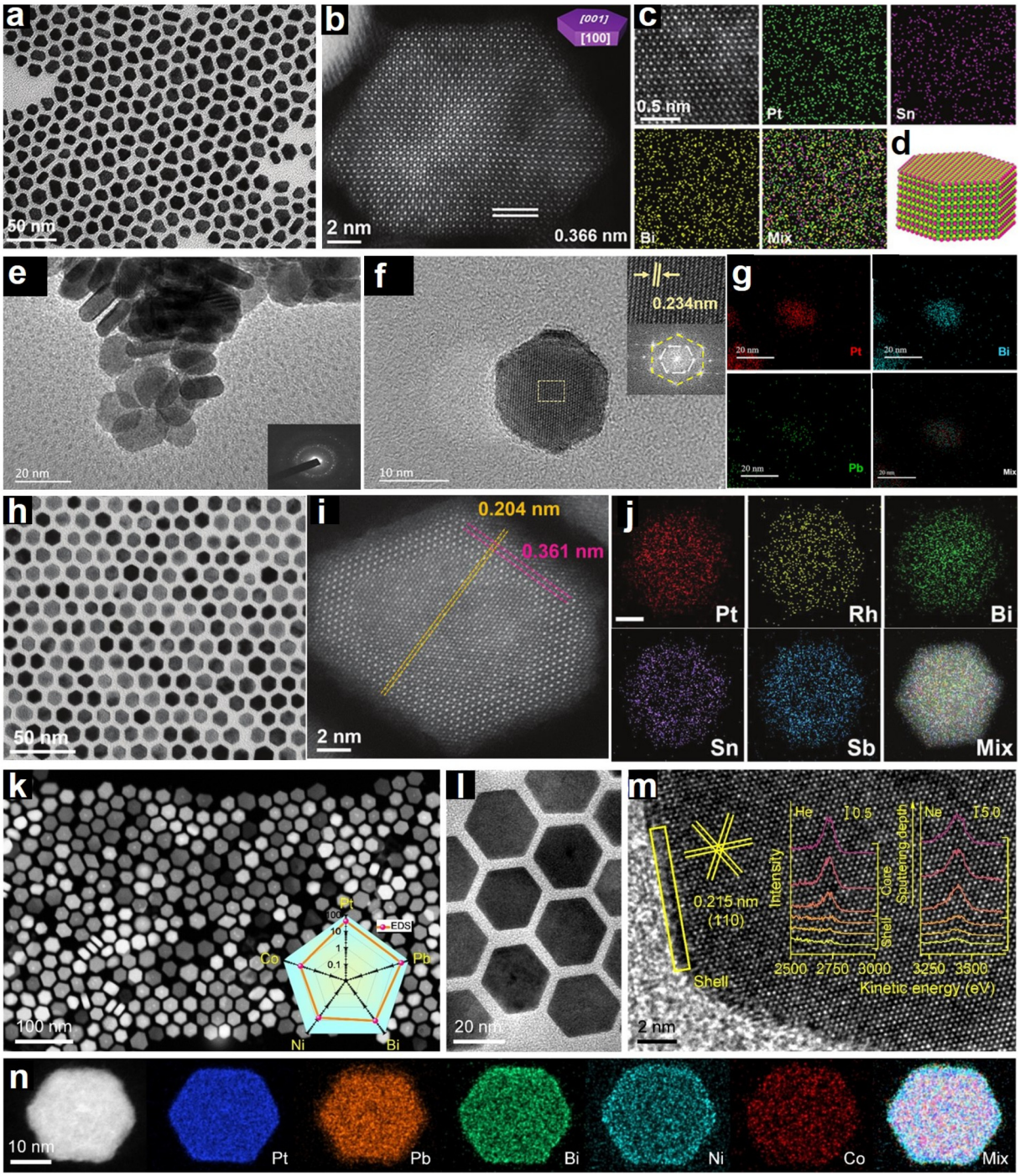

Fig. 4 (a) TEM and (b) HRTEM images, (c) atomic-resolution EDX mapping, and (d) schematic illustration of 2D PtSnBi IMNPs. Green, purple, and yellow spheres represent Pt, Sn, and Bi atoms, respectively. This figure has been adapted from ref. 65 with permission from John Wiley and Sons, copyright 2019. (e) TEM and (f) HRTEM images and (g) EDX mapping of 2D intermetallic PtPbBi HNPs. This figure has been adapted from ref. 66 with permission from the American Chemical Society, copyright 2020. (h) TEM, (i) HAADF-STEM, and (j) EDX mapping images of high-entropy 2D PtRhBiSnSb IMNPs. This figure has been adapted from ref. 67 with permission from John Wiley and Sons, copyright 2022. (k) HAADF-STEM image. Inset shows the HAADF-STEM-EDX results for an individual high-entropy 2D PtBiPbNiCo NP. (l) TEM image and (m) HRTEM image of high-entropy 2D PtBiPbNiCo IMNPs. (n) Elemental mappings. This figure has been adapted from ref. 68 with permission from John Wiley and Sons, copyright 2023.

(100) planes in PtBi (0.374 nm), PtSn (0.355 nm) and PtSb (0.358 nm) intermetallic compounds. In addition, the consistent lattice spacing of 0.204 nm indicates identical *hcp* crystal structures across the NPs. The EDX mapping results in Fig. 4j reveal that the atomic percentages of Rh and Bi are higher in the central parts of the NPs, and the atomic percentages of Pt,

Sn, and Sb are higher near the NP edges. Huang and co-workers obtained high-entropy 2D PtBiPbNiCo HNPs with an average diameter of 26.2 ± 3.3 nm and an average thickness of 8.4 ± 1.5 nm by reacting 9.8 mg $Pt(acac)_2$, 2.5 mg $NiCO_3{\cdot}2Ni(OH)_2$, 2.6 mg $2CoCO_3{\cdot}3Co(OH)_2$, 8.0 mg $Pb(acac)_2$, 7.5 mg $(BiO)_2CO_3$, and 53.4 mg AA in 2.5 mL OAm and 2.5 mL ODE at 180 °C for 5 h, as shown in the TEM images in Fig. 4k and l.[68] HAADF-STEM-EDX analysis of an individual NP shows that the Pt/Pb/Bi/Ni/Co composition is around 41.7 : 33.4 : 10.8 : 6.3 : 7.8 (inset of Fig. 4k). The HRTEM image shows a lattice distance of 0.215 nm, which corresponds to the lattice distance of the PtPb (110) facet, as shown in Fig. 4m. A distinct core–shell structure could be observed, where the abrupt changes of elemental signals could be detected in the ion scattering spectrum (ISS, inset of Fig. 4m). Moreover, aberration-corrected HAADF-STEM-EDX elemental mappings in Fig. 4n show that each element is uniformly distributed.

3.1.2. 2D Pd-based intermetallic nanosheets

3.1.2.1 2D Pd–Pb intermetallic nanosheets. Huang *et al.* reported the fabrication of 2D Pd_3Pb/Pd core/shell IMNSs by reacting 8.9 mg $Pd(acac)_2$, 2.5 mg $Pb(HCOO)_2$, and 60 mg glucose in 4 mL OAm and 1 mL ODE solution at 160 °C for 5 h (Fig. 5a–g).[69] Fig. 5a shows the model of an individual 2D Pd_3Pb/Pd core/shell IMNS imaged from the top-down view. Fig. 5b is the corresponding TEM image of an individual 2D Pd_3Pb/Pd core/shell IMNS from an out-of-plane view. Fig. 5c shows the HAADF-STEM image and corresponding elemental mappings of an individual 2D Pd_3Pb/Pd core/shell IMNS with uniform distributions of Pd and Pb. The HRTEM image of an individual 2D Pd_3Pb/Pd core/shell IMNS is imaged from the

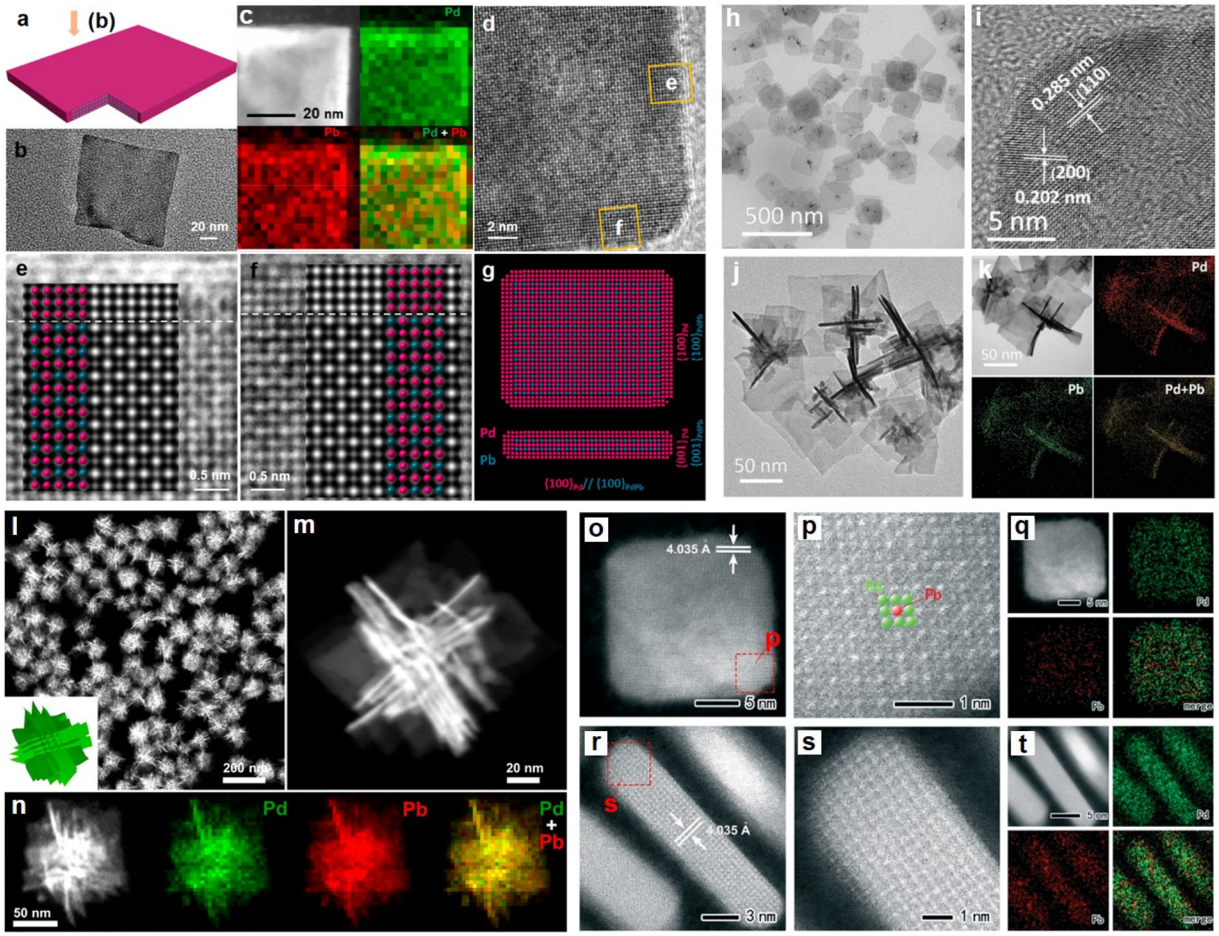

Fig. 5 (a) A model, (b) TEM image from the out-of-plate view, (c) corresponding elemental mappings, and (d) HRTEM image of the 2D Pd_3Pb/Pd core/shell IMNSs. (e and f) HRTEM images from the selected areas in (d). (g) The schematic atom models of the 2D Pd_3Pb/Pd core/shell IMNSs showing the top interface [{100}Pd//{100}Pd_3Pb] and the side interface [(001)Pd//(001)Pd_3Pb]. This figure has been adapted from ref. 69 with permission from the American Chemical Society, copyright 2019. (h) TEM and (i) HRTEM images of Pd_3Pb SNP. (j) Representative TEM and (k) TEM-EDX elemental mapping images of Pd_3Pb NPA-3. This figure has been adapted from ref. 70 with permission from John Wiley and Sons, copyright 2018. (l and m) HAADF-STEM and (n) EDX elemental mapping images of Pd_3Pb NSAs. This figure has been adapted from ref. 71 with permission from the American Chemical Society, copyright 2018. (o and r) HADDF-STEM, (p and s) atomic-resolution HADDF-STEM, and (q and t) EDX mapping images of the planar and vertical Pd_3Pb IMNSs, respectively. This figure has been adapted from ref. 72 with permission from the Royal Society of Chemistry, copyright 2019.

[001] Pd_3Pb zone axis (top view) as shown in Fig. 5d. Fig. 5e and f are HRTEM images taken at higher magnifications and the corresponding simulated images from the areas indicated by the yellow rectangles in Fig. 5d. Obviously different stacking sequences in the HRTEM images demonstrate Pd (layer) and Pd_3Pb (core). As a result, a large tensile strain was produced because the lattice parameter of the Pd shell was smaller than that of intermetallic Pd_3Pb. In addition, pure Pd_3Pb IMNSs without the Pd layer were obtained by decreasing the amount of $Pd(acac)_2$ from 8.9 mg to 7.6 mg. Guo *et al.* reported the synthesis of intermetallic Pd_3Pb square NPs (SNP) enclosed by {100} facets with a thickness of 5.2 nm *via* reaction with 7.6 mg $Pd(acac)_2$, 32 mg $Pb(acac)_2$, 35.6 mg L-ascorbic acid (AA), and 25 mg NH_4Br in 2.5 mL OAm and 2.5 mL ODE solution at 100 °C for 120 min (Fig. 5h and i).[70] NH_4Br is indispensable for forming Pd_3Pb SNPs due to the strong selective bonding of Br^- on the {100} facet of *fcc* Pd_3Pb. When the content of $Pb(acac)_2$ was changed from 32 mg to 24, 16, 8, and 4 mg, the morphologies of Pd_3Pb changed from SNP to NP assemblies (NPA, named NPA-4, NPA-3, NPA-2, and NPA-1, respectively) with decreased {100} facet orientation (Fig. 5j and k). Huang *et al.* reported the fabrication of intermetallic Pd_3Pb nanosheet assemblies (NSAs) with a thickness of 3.25 nm *via* reaction with 7.6 mg of $Pd(acac)_2$, 4.0 mg of $Pb(acac)_2$, 5.4 mg of $FeCl_3{\cdot}6H_2O$, and 40.0 mg of phloroglucinol in 4.0 mL OAm and 1.0 mL oleic acid (OA) solution at 100 °C for 5 h (Fig. 5l–n).[71] The HAADF-STEM images in Fig. 5l and m indicated that the highly dispersed Pd_3Pb NSAs were composed of many 2D ultrathin NSs. Zhang *et al.* reported the fabrication of Pd_3Pb IMNPs with a thickness of 4.4 nm by reacting 0.06 mM $Pd(acac)_2$ and 0.02 mM $Pb(acac)_2$ in a mixture of 4 mL of OAm, 1 mL of ODE, and 1 mL of OA at 180 °C for 1.5 h (top view: Fig. 5o–q, side view: Fig. 5r–t).[72] In addition, the absence of OA will lead to Pd_3Pb alloy dendritic nanocrystals. It was also reported that Pd_3Pb IMNS constructed flowers were obtained by reacting 0.06 mM $Pd(acac)_2$, 0.02 mM $Pb(acac)_2$, 30 mg AA, and 60 mg CTAC in 5 mL of OAm at 200 °C for 1.5 h.[73]

3.1.2.2 2D Pd–Zn intermetallic nanosheets. Zhang and coworkers reported the use of 13.95 mg $Mo(CO)_6$ to reduce 6.12 mg $Pd(acac)_2$ and 6.36 mg $Zn(acac)_2{\cdot}xH_2O$ with a molar ratio of 1.0 : 1.2 in 6 mL OAm solution to prepare ultrathin PdZn IMNSs with a thickness of only 3 nm and an unconventional *fct* phase at 325 °C for 30 min (Fig. 6a–e).[74] CO released from $Mo(CO)_6$ at high temperature serves as the capping agent for the synthesis of PdZn IMNSs. The TEM images in Fig. 6(a and b) confirm the high purity of 2D NSs. HAADF-STEM-EDX elemental mapping results in Fig. 6c revealed the uniform distribution of Pd and Zn elements. The X-ray diffraction (XRD)

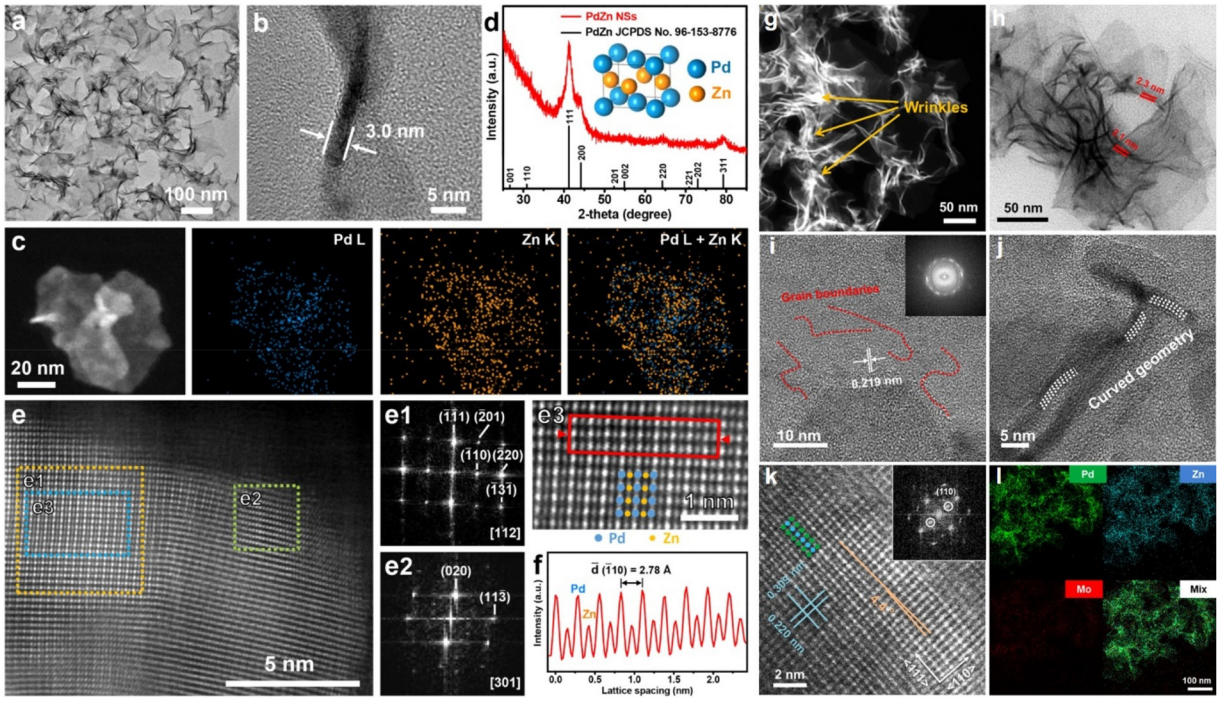

Fig. 6 (a and b) TEM images of PdZn IMNSs. (c) HAADF-STEM image and the corresponding EDX elemental mapping images. (d) XRD pattern and (e) aberration-corrected HAADF of PdZn IMNS. (e1 and e2) FFT patterns taken from the orange and green dotted squares marked as e1 and e2 in (e). (e3) Magnified aberration-corrected HAADF-STEM image from the blue dotted rectangle marked as e3 in (e). (f) Line intensity profile taken along the atomic layers in the red rectangle in (e3). This figure has been adapted from ref. 74 with permission from the American Chemical Society, copyright 2019. (g) TEM and (h) HAADF-STEM images of L10–Mo–PdZn IMNSs. HRTEM images of L10–Mo–PdZn NSs from (i) lateral and (j) folded edge regions. (k) Atomic resolution HAADF-STEM image of L10–Mo–PdZn IMNSs. Inset is the corresponding FFT pattern. (l) STEM-EDX elemental mappings of Pd, Zn, and Mo of L10–Mo–PdZn IMNSs. This figure has been adapted from ref. 75 with permission from John Wiley and Sons, copyright 2022.

pattern in Fig. 6d is in good accordance with the *fct*-PdZn phase. The HAADF-STEM image in Fig. 6e and line intensity profile in Fig. 6f further confirmed the intermetallic *fct*-PdZn phase. The temperature plays an important role due to the great difference in reduction potentials between Pd^{2+}/Pd (0.95 V *vs.* standard hydrogen electrode (SHE)) and Zn^{2+}/Zn (−0.76 V *vs.* SHE). Zn^{2+} was fully reduced at a reaction temperature of 250 °C and above, resulting in the formation of PdZn IMNSs with a Pd : Zn ratio close to 1 : 1. PdZn NSs with *fcc* phase and lower Zn content were obtained when the reaction temperature was below 250 °C. Li *et al.* reported the preparation of Mo-doped L10-PdZn IMNSs with a thickness of only 2.1 nm (7–10 atomic layers) by reacting 7.8 mg $Pd(acac)_2$, 8 mg $Zn(acac)_2$, and 30 mg $Mo(CO)_6$ in 6 mL OAm at 300 °C for 2 h (Fig. 6g–l).[75] The TEM image in Fig. 6g and HAADF-STEM image in Fig. 6h confirm that 2D NSs with lengths up to several hundred nanometers are the dominant product and obvious winkles can be clearly observed within L10–Mo–PdZn IMNSs. The lattice fringe spacing is found to be 0.219 nm from the HRTEM image of the lateral region in Fig. 6i, corresponding to the (111) facet of L10–PdZn and several grain boundaries can be clearly observed. The corresponding FFT pattern also confirms the poly-crystalline nature of L10–Mo–PdZn IMNSs. In addition, the curved geometry is further evidenced in the HRTEM image of the folded edge region in Fig. 6j, where the distortion of lattice fringes along the curved edge is clearly observed. Fig. 6k is the atomic-scale structure of L10–Mo–PdZn IMNSs. A clear periodic arrangement of bright (Pd) and dark (Zn) atoms is observed, which is in good agreement with the standard L10 structure. A 4.4° lattice distortion can be identified as a result of the curved geometry and is in accordance with Fig. 6j. The (110) superlattice spots are observed in the inset of Fig. 6k. The lattice fringe spacings are found to be 0.309 and 0.220 nm, corresponding to the (110) and (111) facets, respectively. HAADF-STEM-EDX elemental mappings of L10–Mo–PdZn NSs in Fig. 6l demonstrate the uniform distribution of Pd, Zn, and Mo elements throughout the whole NSs.

3.1.2.3 2D Pd–Sb intermetallic sheets. Huang and co-workers reported the synthesis of Pd–Sb HNPs with a thickness of 15.3 nm and ordered rhombohedral Pd_8Sb_3 phase (denoted as Pd_8Sb_3 HNPs) by reacting 7.6 mg $Pd(acac)_2$, 2.1 mg $SbCl_3$, 100.0 mg PVP, and 24.0 mg NH_4Br in 10 mL benzyl alcohol solution at 180 °C for 3 h as shown in the HAADF-STEM images in Fig. 7(a and b).[76] The HAADF-STEM-EDX mappings in Fig. 7b show that the Pd and Sb elements are distributed evenly throughout the whole HNPs. The HAADF-STEM images with atomic resolution obtained from the center and edge of an individual HP are shown in Fig. 7(c–e). It is recognized that the Pd_8Sb_3 HNPs possess the atomic structure of the R_3 space group and with an [001] orientation. Atomic columns with brighter contrast are observed in both Fig. 7d and e, which is in agreement with the atomic model of Pd_8Sb_3. In addition, Pd terminations are observed in Fig. 7e. Fig. 7f is the unit-cell atomic model of Pd_8Sb_3, which is superimposed on Fig. 7d and e. Fig. 7g shows the structure of the Pd_8Sb_3 HNP for the side view of an individual HNP. Fig. 7h is the enlarged area of the dashed box in Fig. 7g, where the structure can be well matched with the Pd_8Sb_3 atomic model viewed along the [−110] direction. Overall, the HAADF-STEM results in Fig. 7(d, e and h) verified the synthesized HP has a perfect Pd_8Sb_3 structure, and the surface planes are {001} while the edge planes are {-110} as shown in Fig. 7i.

3.1.2.4 2D Pd–Cd intermetallic sheets. Additionally, Zhang and co-workers obtained 2D PdCd IMNSs with *fct* phase and a thickness of 4.8 nm by reacting 6.12 mg $Pd(acac)_2$, 5.35 mg Cd $(ac)_2{\cdot}xH_2O$ and 13.95 mg $Mo(CO)_6$ in 6 mL OAm solution at 250 °C for 30 min as shown in the TEM images in Fig. 8(a and b).[74] HAADF-STEM-EDX elemental mapping results in Fig. 8c indicate the even distributions of Pd and Cd elements. The XRD pattern in Fig. 8d shows that the crystal structure is in good accordance with the *fct*-PdCd phase. However, it is hard to distinguish Pd atoms from Cd atoms in the aberration-corrected HAADF-STEM image *via* the *Z*-contrast since the atomic numbers of Pd and Cd are very similar (Z_{Pd} = 46, Z_{Cd} = 48) as shown in Fig. 8e. Fortunately, the FFT patterns (Fig. 8e1 and e2) of different crystalline domains are in accordance with the *fct* phase.

3.1.2.5 Polynary 2D Pd-based intermetallic nanosheets. Zhang *et al.* reported the synthesis of polynary 2D PdZnCd IMNSs with a thickness of 3.6 nm, as shown in Fig. 9a and b, and the procedure was similar to that of the PdZn IMNSs except that $Pd(acac)_2$, $Zn(acac)_2{\cdot}xH_2O$ and $Cd(ac)_2{\cdot}2H_2O$ with different molar ratios were added and the reaction temperature was maintained at 300 °C for 30 min.[74] The Pd, Zn, and Cd elements are evenly distributed in the obtained polynary 2D PdZnCd IMNSs according to the HAADF-STEM-EDX elemental mapping images in Fig. 9c. The crystal structure of PdZnCd IMNSs was further examined by XRD. The XRD results in Fig. 9d confirm that the 2D PdZnCd IMNSs exhibit a similar pattern to those of *fct* PdZn and PdCd and the position of the (111) peak is located between those of PdZn and PdCd. In addition, the aberration-corrected HAADF-STEM image (Fig. 9e), corresponding FFT pattern (Fig. 9f), and the line intensity profile (Fig. 9g) demonstrate that the 2D PdZnCd IMNSs exhibit a typical [100] orientation of the *fct* phase with an average (001) distance of 0.329 nm.

3.2. Seed-mediated synthesis

3.2.1. 2D Pd–Pb intermetallic nanosheets. Huang *et al.* successfully prepared Pd_3Pb ultrathin porous intermetallic nanosheets (UPINs) by using Pd NSs as seeds.[77] The Pd NSs seeds with an average lateral size of 73.9 nm and thickness of 1.6 nm were obtained by reacting 50 mg of $Pd(acac)_2$, 154.6 mg of PVP, and 185 mg of CTAB in 10 mL of benzyl alcohol under 1 bar CO at 30 °C for only 12 h. After that, Pd_3Pb UPINs were obtained by reacting 1.42 mg Pd NSs, 80 mg of AA, and 1.8 mg of $Pb(acac)_2$ in 4 mL of OAm solution at 140 °C for only 10 min, as shown in Fig. 10. The representative HAADF-STEM image in Fig. 10a indicated that the resultant product was dominated by a 2D porous nanostructure. Their average lateral size and thickness were estimated to be 61.4 nm (Fig. 10b) and 2.6 nm (Fig. 10c). The XRD pattern in Fig. 10d corroborates the

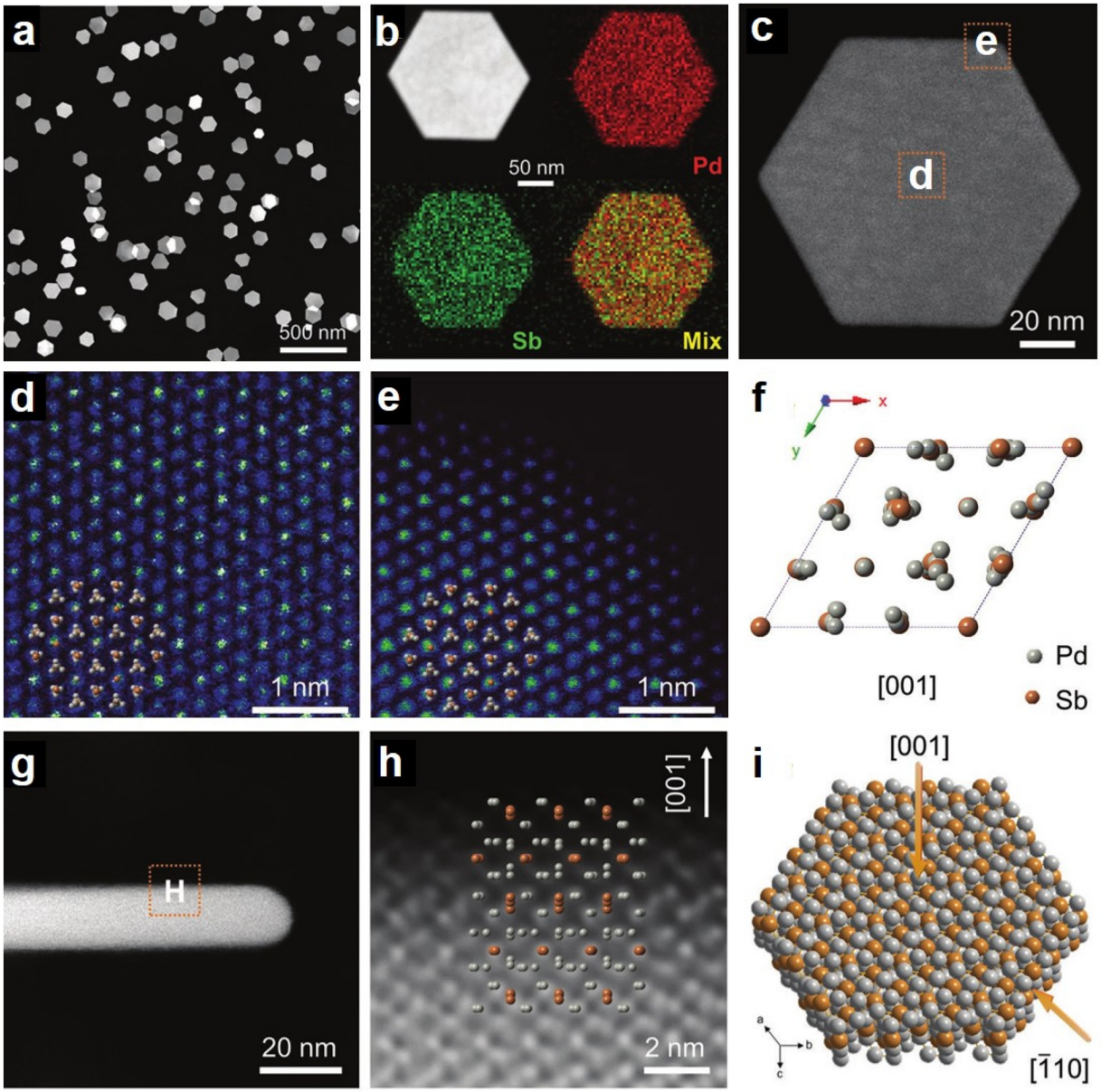

Fig. 7 (a) HAADF-STEM image and (b) the corresponding EDX elemental mapping images of 2D Pd_8Sb_3 HNPs. (c) Low-magnification HAADF-STEM image and (d and e) high-resolution HAADF-STEM images taken from areas in (c). (f) The solved crystal structure model viewed along the [001] direction. (g) Low-magnification and (h) high-resolution HAADF-STEM images of side-viewed individual HNP loaded on carbon nanotubes. (i) Schematic diagram showing the two observation directions. This figure has been adapted from ref. 76 with permission from John Wiley and Sons, copyright 2022.

intermetallic Pd_3Pb cubic phase. The Pd : Pb ratio of Pd_3Pb UPINs was determined to be 75.6 : 24.4 by inductively coupled plasma-atomic emission spectroscopy (ICP-AES); this ratio was very close to the value (76.3 : 23.7) estimated from the STEM-EDX spectrum in Fig. 10e. As shown in Fig. 10f, the atomic-resolution HAADF-STEM image displays the periodic brightness contrast due to the obvious *Z*-contrast difference between Pb (Z = 82) and Pd (Z = 46), proving the atomically ordered intermetallic structure. The corresponding intensity profiles in Fig. 10g also demonstrate the ordered atomic arrangement of Pd and Pb atoms. The STEM-EDX elemental mapping results, as shown in Fig. 10h, clearly reveal that Pd and Pb elements are evenly distributed throughout the UPINs. The high-resolution X-ray photoelectron spectroscopy (XPS) results in Fig. 10i further demonstrate that the majority of Pd and Pb is in a metallic state. The porous structure was attributed to the fragmentation of ultrathin Pd NSs caused by the intensified oxidative etching reaction at high temperature, which selectively dissolved those defect sites on Pd NSs and thus broke the NSs into fragile NSs. The subsequently produced Pb atoms were deposited on the Pd NSs, which further triggered the interatomic diffusion (including the migration of

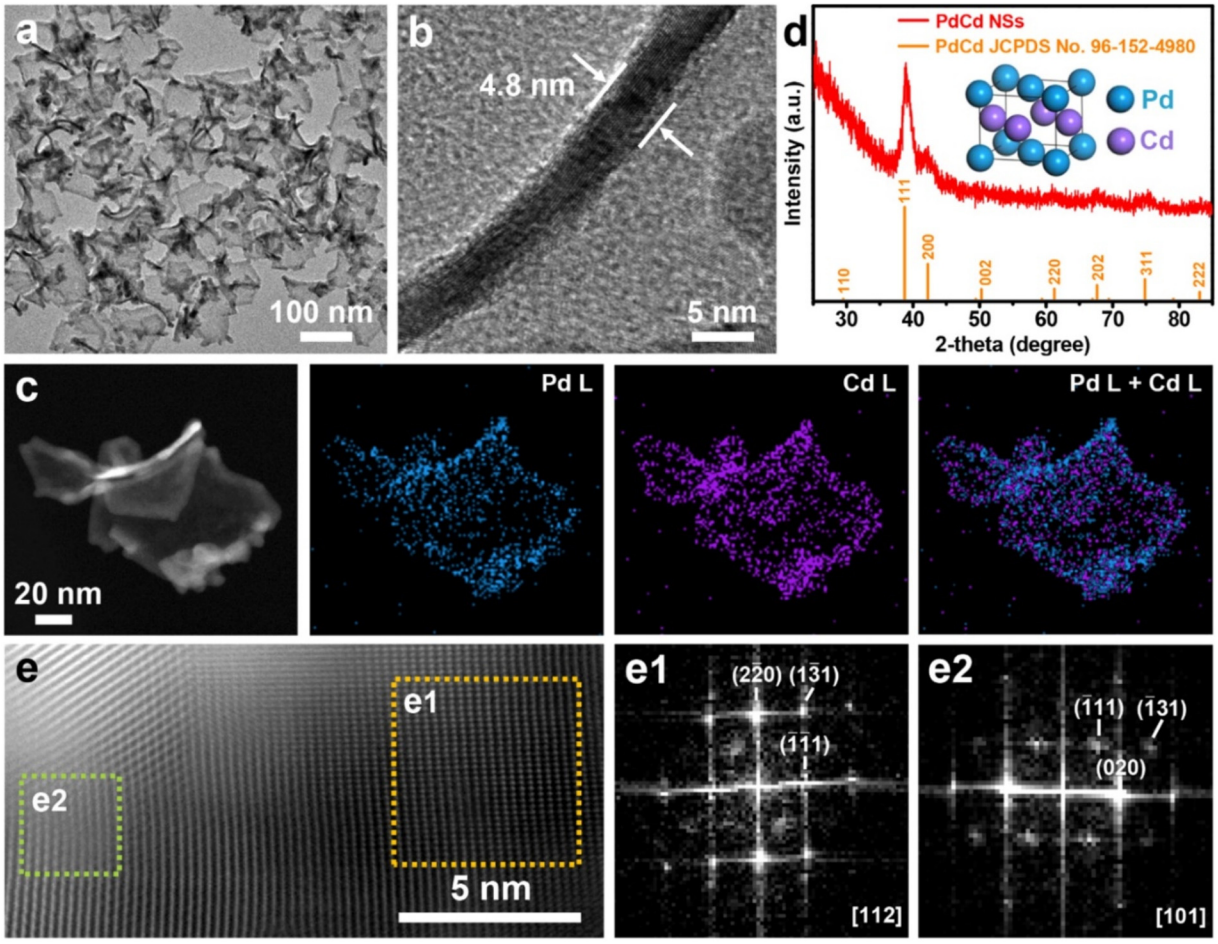

Fig. 8 (a and b) TEM images of 2D PdCd IMNSs. (c) HAADF-STEM image and the corresponding EDX elemental mapping images. (d) XRD pattern of PdCd NSs. (e) Aberration-corrected HAADF-STEM image of a typical PdCd IMNS. (e1 and e2) FFT patterns taken from the orange and green dotted squares marked as e1 and e2 in (e). This figure has been adapted from ref. 74 with permission from the American Chemical Society, copyright 2019.

Pd atoms) and ordering process driven by the reduction in Gibbs free energy to form the Pd_3Pb UPINs.

3.2.2. 2D Pd–Sn intermetallic nanosheets. In addition, Huang *et al.* obtained 2D Pd_3Sn UPINs by replacing $Pb(acac)_2$ with $SnCl_2$ at 180 °C for 10 min (Fig. 11a–f).[77] The 2D Pd_3Sn UPINs have an average thickness of 2.6 nm, as determined from the TEM images (Fig. 11a and b). The corresponding XRD patterns in Fig. 11c confirm the intermetallic Pd_3Sn phase. However, the atomic-resolution HAADF-STEM image in Fig. 11d displays an obscure periodic brightness contrast due to the inconspicuous *Z*-contrast differences between Pd (Z = 46) and Sn (Z = 50). Even for that, the corresponding intensity profile for Pd_3Sn UPINs in Fig. 11e still testifies to the ordered atomic arrangement of Pd and Sn atoms. Furthermore, the homogeneous distributions of Pd and Sn elements throughout the UPINs were revealed by STEM-EDX elemental mapping profiles, as shown in Fig. 11f. Additionally, Li *et al.* also obtained Pd NSs with a thickness of 1.6 nm by reacting 7.8 mg $Pd(acac)_2$ and 36 mg CTAB in 5 mL OAm solution under a CO atmosphere at 160 °C for 40 min.[78] The subsequent ultrathin channel-rich ordered Pd_2Sn (o-Pd_2Sn) IMNSs with a thickness of 3.5 nm were synthesized by reacting the prepared Pd NSs, 8 μL $Sn(Buty)_2(acac)_2$, and 100 mg citric acid (CA) in 5 mL OAm at 170 °C for 120 min (Fig. 11g–i). The TEM (Fig. 11g) and HAADF-STEM (Fig. 11h) images show that abundant channels can be observed in o-Pd_2Sn IMNSs. The HAADF-STEM-EDX elemental mapping images (Fig. 11i) of a single o-Pd_2Sn NS reveal the uniform distribution of Pd and Sn elements throughout the IMNS. Besides, disordered Pd_4Sn NSs (d-Pd_4Sn NSs) were also prepared at 160 °C for 120 min as a control sample.

3.2.3. 2D Pd–Cd intermetallic nanosheets. As reported by Huang *et al.*, PdCd UPINs were obtained by replacing $Pb(acac)_2$ with $C_4H_6CdO_4$ at 250 °C for 10 min (Fig. 12a–h).[77] The 2D Pd_3Cd UPINs have an average thickness of 2.7 nm, as determined from the TEM images (Fig. 12a and b). The corresponding XRD patterns in Fig. 12c confirm the intermetallic PdCd phase. However, the atomic-resolution HAADF-STEM image in Fig. 12d displays an obscure periodic brightness contrast due to the inconspicuous *Z*-contrast differences between Pd (Z = 46) and Cd (Z = 48). Together with the measured lattice spacing of 0.23 nm assigned to the {111} planes of the PdCd intermetallic phase, the FFT pattern (Fig. 12e), and the inten-

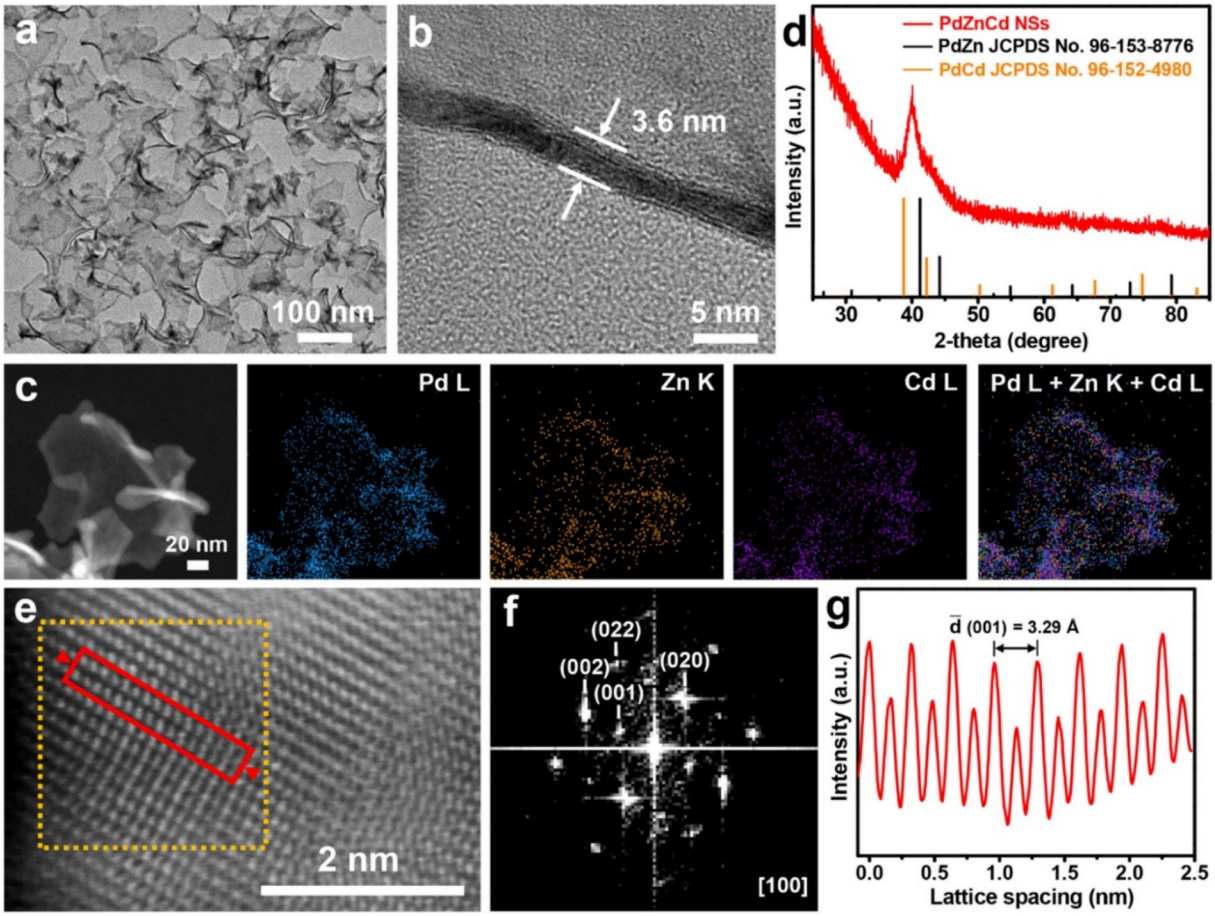

Fig. 9 (a and b) TEM images of PdZnCd IMNSs. (c) HAADF-STEM image and the corresponding EDX elemental mapping images. (d) XRD pattern of PdZnCd NSs. (e) Aberration-corrected HAADF-STEM image of a typical PdZnCd IMNS. (f) FFT pattern taken from the orange dotted square in (e). (g) Line intensity profile taken along the atomic layers in the red rectangle in (e). This figure has been adapted from ref. 74 with permission from the American Chemical Society, copyright 2019.

sity profile (Fig. 12f and g), the periodic arrangement of Pd and Cd atoms was confirmed. Furthermore, the homogeneous distributions of Pd and Cd elements throughout the UPINs were revealed by STEM-EDX elemental mapping profiles, as shown in Fig. 12h.

3.3. One-pot synthesis and seed-mediated synthesis

Quan and co-workers synthesized trace Pd-modified intermetallic PtBi IMNPs (PtBi@Pd IMNPs) by a two-step solution-based co-modification strategy.[79] In the first step, the PtBi hexagonal IMNPs were firstly synthesized as seeds by reacting 20.4 mg of $Pt(acac)_2$, 20.0 mg of $Bi(act)_3$, 80 mg of AA, and 350 mg of CTAB in 5 mL of OAm and 5 mL of ODE at 220 °C for 1 h. In the second step, different amounts of $Pd(acac)_2$ in OAm and ODE solution were added very slowly and the reaction temperature was maintained at 190 °C for 1 h to obtain three Pd-modified PtBi IMNPs (PtBi@0.9% Pd IMNPs, PtBi@1.8%Pd IMNPs, and PtBi@3.0%Pd IMNPs). Fig. 13 shows the HAADF-STEM (Fig. 13a), corresponding EDX elemental mapping (Fig. 13b), and atomic resolution HAADF-STEM (Fig. 13c) images of PtBi@1.8%Pd IMNPs. The average edge length of PtBi@1.8% Pd IMNPs is 6.7 ± 0.5 nm, and the average thickness is determined to be 7.7 ± 1.2 nm. The profile of the brightness intensity (Fig. 13d) along the red line in Fig. 13c contains two strong peaks, while the green line profile (Fig. 13f) with the same length contains similar six peaks, demonstrating two different atomic arrangements of the PtBi@1.8%Pd IMNPs. The lattice spacing of the crystal planes is found to be 0.375 nm in the red rectangle of Fig. 12c, which is ascribed to *hcp*-PtBi viewed along the [001] zone axis, and the corresponding crystal model is shown in Fig. 13e. In contrast, the interplanar spacings are found to be 0.236 nm and 0.228 nm in the green rectangle of Fig. 13c, which are identified as crystal planes (111) and (002) and considered as *fcc*-Pd viewed along the [110] zone axis, and the corresponding crystal model is shown in Fig. 13g. In fact, the discontinuous *fcc*-Pd islands/clusters should be located on the surface of *hcp*-PtBi in PtBi@1.8%Pd IMNPs. In addition, Quan and co-workers prepared PtBi@6.7%Pb IMNPs by adding 11.0 mg Pb $(acac)_2$ to a solution of pre-synthesized PtBi IMNPs maintained at 260 °C for 1 h.[80] The *hcp* structure is clearly demonstrated by the rhomboid periodic patterns viewed along the [001] zone

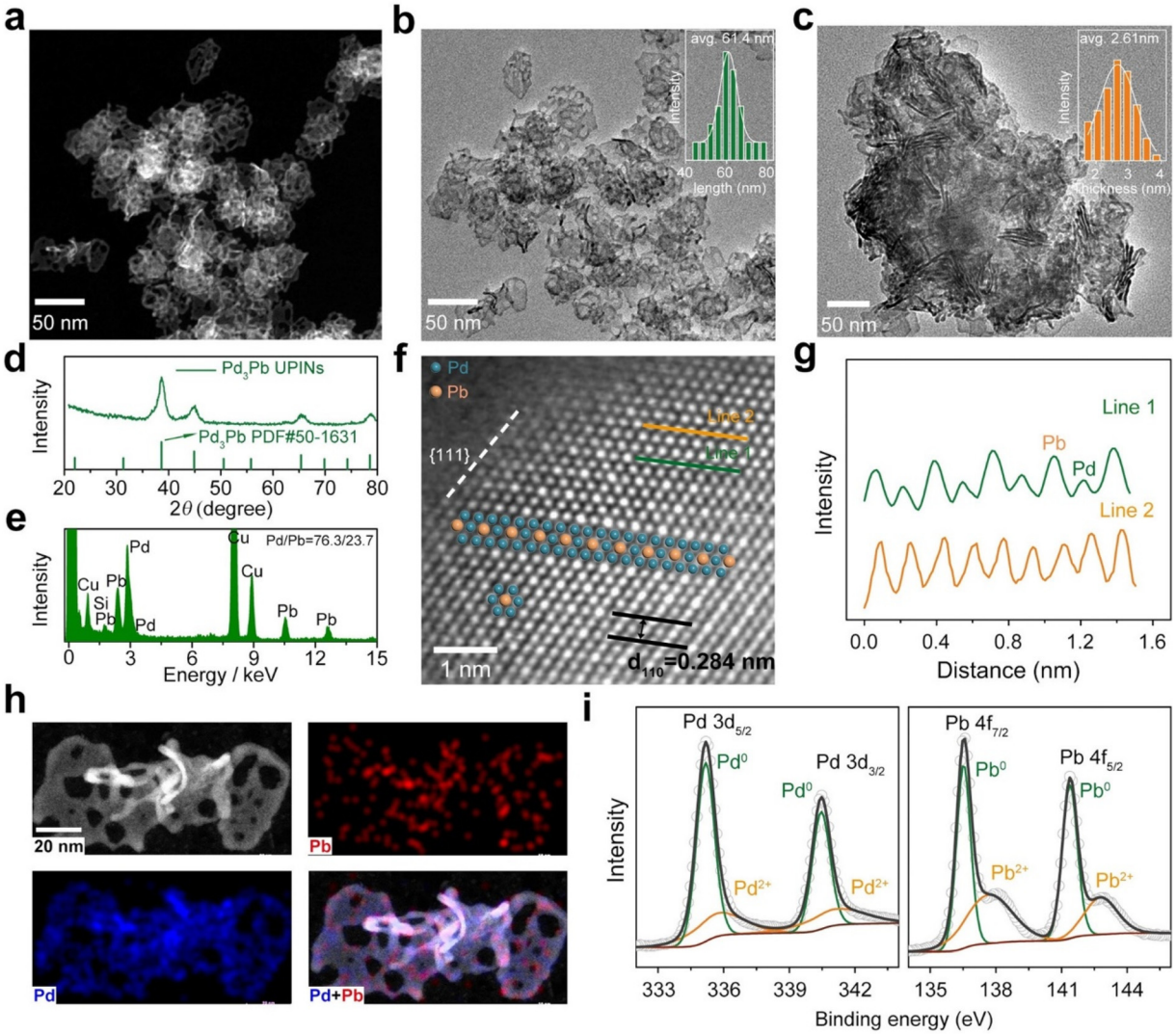

Fig. 10 Structural and compositional characterization of intermetallic Pd_3Pb UPINs. (a) HAADF-STEM image. (b) and (c) Low-magnification TEM images. The insets in (b) and (c) show the corresponding diagonal length and thickness distributions, respectively. (d) XRD pattern. (e) STEM-EDX spectrum. (f) Atomic-resolution aberration-corrected HAADF-STEM image. (g) The intensity profiles taken along the olive and orange lines in (f). (h) STEM-EDX elemental mapping images. (i) XPS of Pd 3d and Pb 4f spectra. This figure has been adapted from ref. 77 with permission from John Wiley and Sons, copyright 2021.

axis, as shown in the aberration-corrected HAADF-STEM image (Fig. 13h), corresponding FFT pattern (Fig. 13i), and enlarged HAADF-STEM image (Fig. 13j). Additional investigations indicated that the Pb atoms were located on the surface, as illustrated in Fig. 13k. In addition, the EDX mapping results in Fig. 13l show the uniform distribution of Pt, Bi, and Pb elements.

4. Electrocatalytic applications in fuel cells

4.1. Oxygen reduction reaction

In contrast to its anodic counterpart, the sluggish reaction kinetics of the cathodic ORR is the largest obstacle to the practical use of PEMFCs due to a higher overpotential requirement to meet the actual current density.[15] Intermetallic nanocatalysts have attracted much attention due to their excellent catalytic activity and stability for the ORR, which arise from the high formation energy and polymetallic composition induced ensemble, ligand, and geometric effects.[16] In addition, even nanocatalysts with the same random alloy composition may exhibit quite different catalytic performances due to their unconfirmed structures with varying electronic structures.[17] In contrast, intermetallic nanocatalysts with well-defined stoichiometry exhibit unique and intriguing physicochemical properties, and serve as ideal platforms for studying the structure-to-property relationships.[22]

Activated carbon-loaded PtBi/Pt core/shell IMNPs (Fig. 2a–d), and commercial Pt/C were evaluated by using a rotating

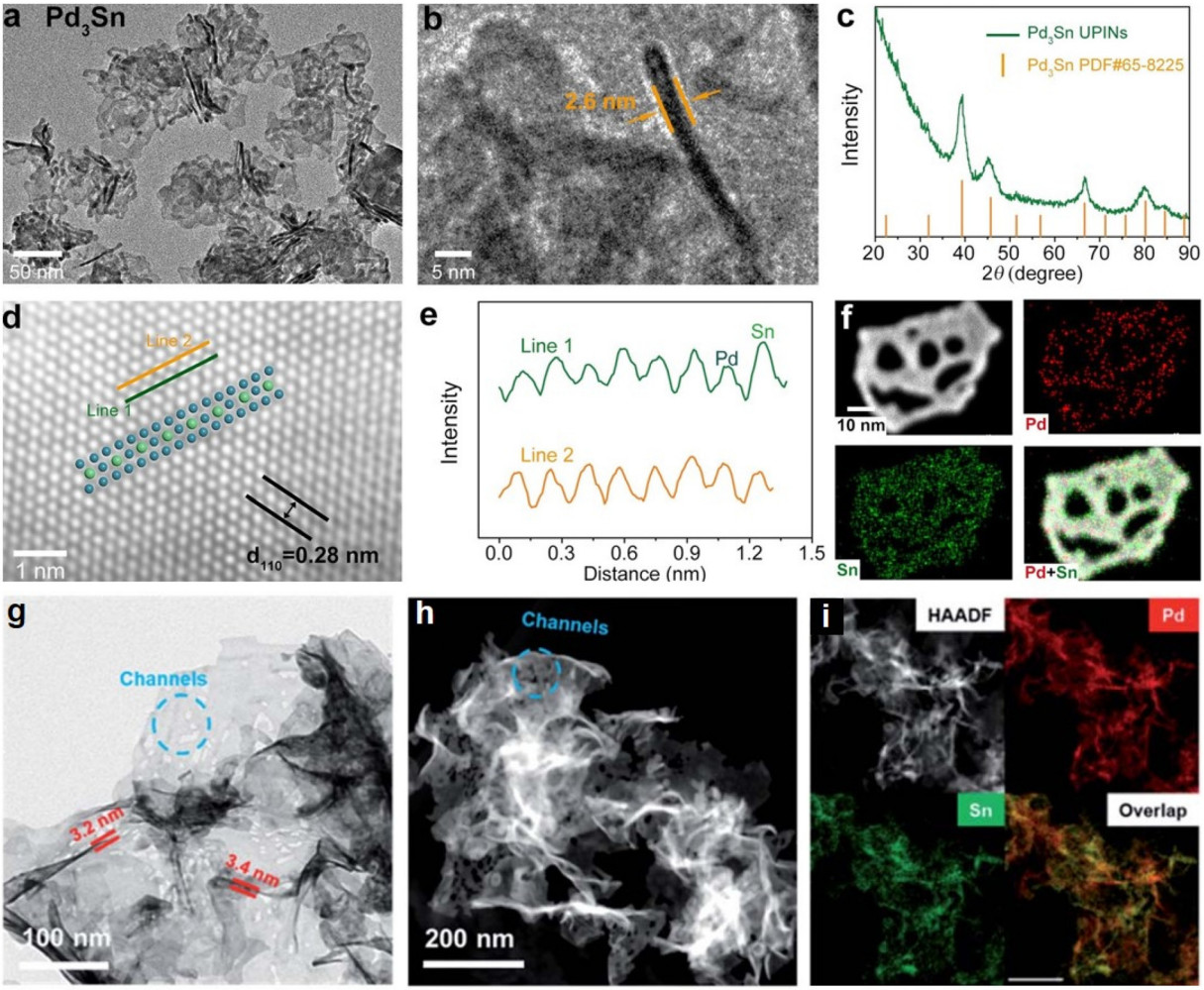

Fig. 11 Structural and compositional characterization of 2D Pd_3Sn UPINs (a–f) and channel-rich o-Pd_2Sn IMNSs (g–i). (a) Low-magnification TEM image. (b) HRTEM image. (c) XRD pattern. (d) Atomic-resolution aberration-corrected HAADF-STEM image. (e) The intensity profiles taken along the olive and orange lines in (d). (f) STEM-EDX elemental mapping images of 2D Pd_3Sn UPINs. This figure has been adapted from ref. 77 with permission from John Wiley and Sons, copyright 2021. (g) TEM, (h) HAADF-STEM, and (i) STEM-EDX elemental mapping images of ultrathin channel-rich o-Pd_2Sn IMNSs. This figure has been adapted from ref. 78 with permission from the Royal Society of Chemistry, copyright 2020.

disk electrode (RDE) in an O_2-saturated 0.1 M $HClO_4$ solution.[57] Firstly, density functional theory (DFT) was used to calculate the free energy pathways for the acidic four-electron ORR based on the systems of PtBi–Pt-interface, PtBi–Pt-edge, PtBi surface, and Pt surface to discuss different uphill (electrode potential U = 0) and downhill (electrode potential U = 1.23 V) behaviors of these four-electron ORR pathways, as shown in Fig. 14a. In an average view, the PtBi/Pt core/shell IMNPs are more energetically favorable to generate $2H_2O$ *via* the ORR. The rate-determining step appears to be the last reduction step, [*OH + H] → H_2O*, with a reaction barrier of 0.8–0.9 eV. From the local structures shown in Fig. 14b, the O-related intermediate molecules simultaneously bond with Bi and Pt sites at the interface, which have higher catalytic activities. Therefore, in the PtBi–Pt interface system, Bi suppresses the Pt–(H, O) overbinding effect, and the efficiency of the adsorption/desorption steps is increased and these steps are barrier-free. With respect to the trends of electronics and energetics, we further confirmed that the interface and edge areas both had high electronic activities and activated the high ORR energetic performance simultaneously. As shown in Fig. 14c, the specific activity (SA) of PtBi/Pt core/shell IMNP/C reaches 1.04 mA cm_{Pt}^{-2} at 0.9 V *vs.* a reversible hydrogen electrode (RHE), which is 5.2 times higher than that of Pt/C. Meanwhile, the mass activity (MA) of PtBi/Pt core/shell IMNP/C was more than 2 times higher than that of Pt/C. Moreover, both the electrochemically active surface areas (ECSAs) and MA of PtBi/Pt core/shell IMNP/C negligibly degrade after 5000 potential cycles of electrochemically accelerated durability tests (ADTs).

Surface strain can modulate the surface electronic structure and alter the interactions between intermediate species and active sites.[81,82] Therefore, strain engineering is an important approach to improve the electrocatalytic performance in fuel cell-relevant reactions. As such, PtPb/Pt core/shell IMNPs with

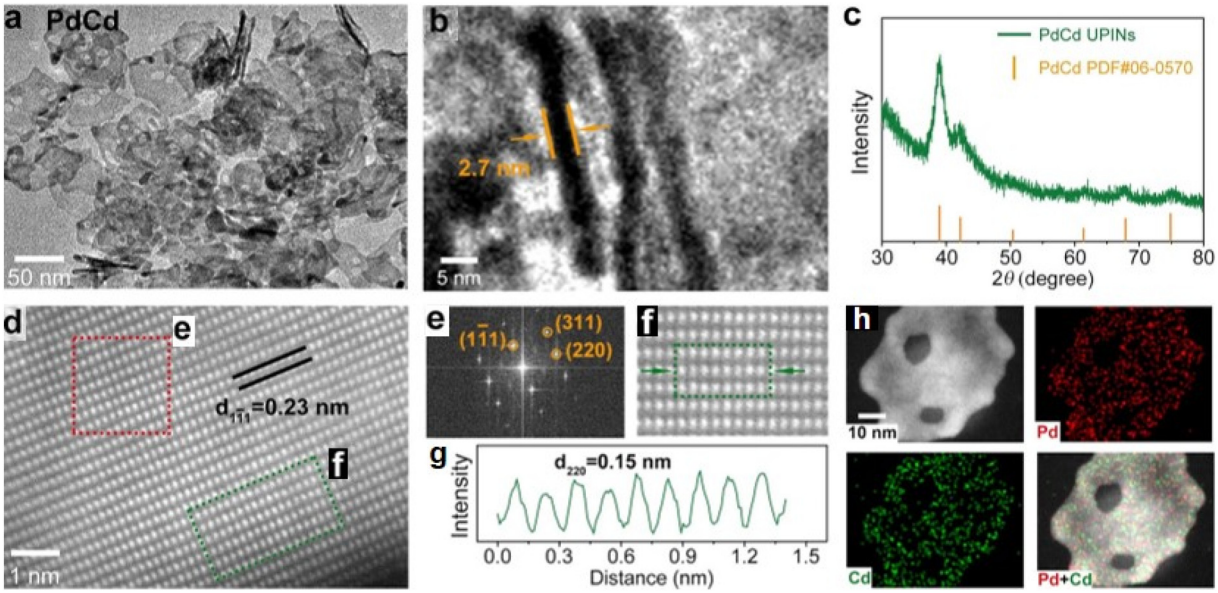

Fig. 12 Structural and compositional characterization of 2D PdCd UPINs. (a) Low-magnification TEM image. (b) HRTEM image. (c) XRD pattern. (d) Atomic-resolution aberration-corrected HAADF-STEM image. (e) FFT pattern taken from the region outlined by the red rectangle in (d). (f) Atomic-resolution HAADF-STEM taken from the region outlined by the green rectangle in (d). (g) The intensity profile taken from the region outlined by green rectangle in (d). (h) STEM-EDX elemental mapping images. This figure has been adapted from ref. 77 with permission from John Wiley and Sons, copyright 2021.

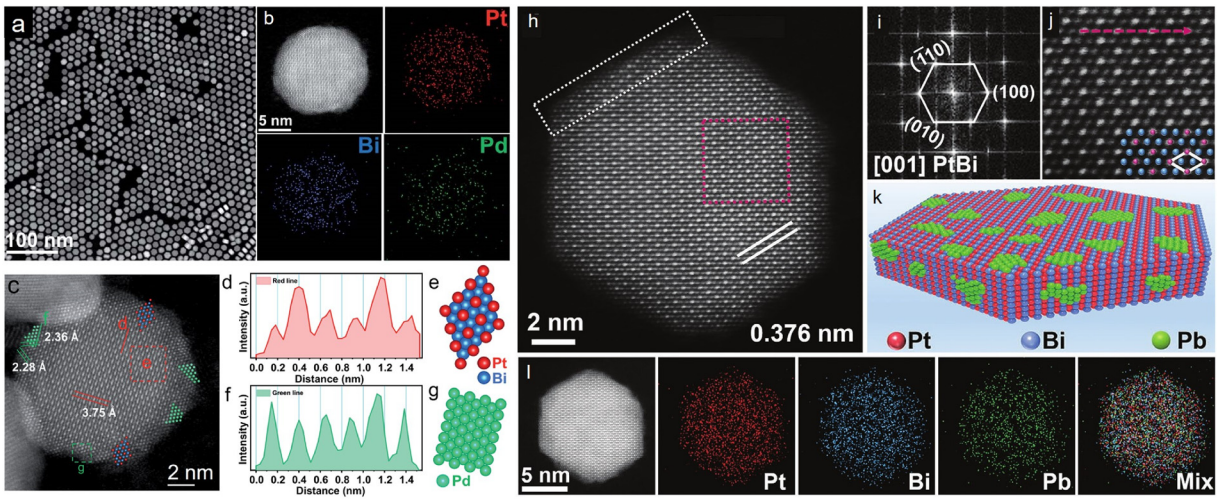

Fig. 13 Structural characterization of PtBi@1.8%Pd (a–g) and PtBi@6.7%Pb (h–l) IMNPs. (a) HAADF-STEM, (b) EDX elemental mapping, and (c) atomic resolution HAADF-STEM images of PtBi@1.8%Pd IMNPs. (d) Profile of brightness intensity along the red line in (c). (e) Crystal model of the lattice region marked with a red frame in (c). (f) Profile of brightness intensity along the green line in (c). (g) Crystal model of the lattice region marked with a green frame. This figure has been adapted from ref. 79 with permission from the Royal Society of Chemistry, copyright 2021. (h) Aberration-corrected HAADF-STEM image and (i) corresponding FFT pattern (viewed along *hcp*-PtBi [001] zone axis) of typical PtBi@6.7%Pb IMNPs. (j) Enlarged HAADF-STEM image from the area indicated by the red dashed rectangle in (h). (k) Schematic illustration showing the atomic arrangement of Pt/Bi/Pb atoms in PtBi@6.7%Pb IMNPs. (l) EDX mapping images of a PtBi@6.7%Pb IMNPs. This figure has been adapted from ref. 80 with permission from John Wiley and Sons, copyright 2022.

large biaxial strains (Fig. 3a–c) were used to investigate the strong tensile strain for ORR enhancement.[61] The oxygen adsorption energy (E_O) was calculated by DFT. It was reported that the ORR activity reached a maximum at some optimal value of E_O.[83] Therefore, the optimal E_O value was shifted to 0 eV and ΔE_O was used to represent the difference of a given E_O value from this optimal reference. Both the SAED and HRTEM results revealed a large tensile strain along [001] and a compressive strain along [110] on both the top-Pt and edge-Pt surfaces of PtPb/Pt core/shell IMNPs. ΔE_O values on the Pt (110)

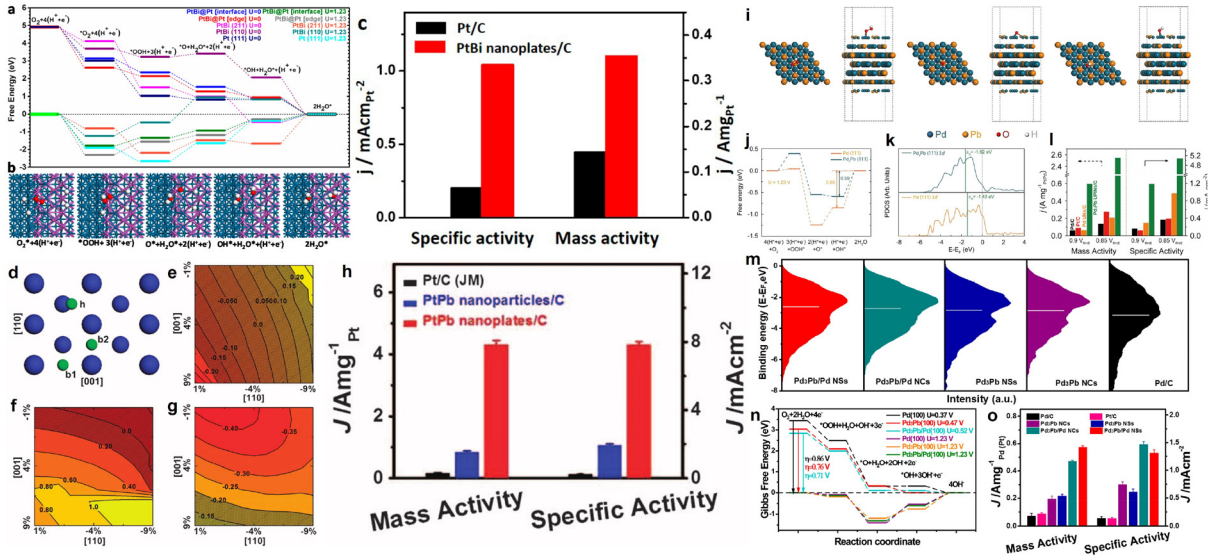

Fig. 14 ORR performances. (a) Free energy pathways for the acidic four-electron ORR based on the systems of PtBi–Pt-interface, PtBi–Pt-edge, PtBi (211), PtBi (110), and Pt (111) surfaces, respectively. The free energy diagrams for the ORR at both zero-electrode potential (U = 0) and equilibrium potential (U = 1.23 V) for discussing different up- and downhill behaviours are illustrated and compared. (b) Evolution of the local structural configurations for the simulated ORR process from the PtBi–Pt interface model system. (c) Comparison of the SAs and MAs of PtBi/C and Pt/C catalysts. This figure has been adapted from ref. 57 with permission from the American Chemical Society, copyright 2018. (d) Atomic models of the Pt (110) surface. Three stable adsorption sites for oxygen: "h", "b1", and "b2". The blue and green spheres represent Pt and O atoms, respectively. (e–g) On the Pt (110) surface, ΔE_O as a function of biaxial strain in the [110] and [001] directions for the "h" site (e), the "b1" site (f), and the "b2" site (g). The optimal ΔE_O value is set to 0. ΔE_O value falling in the shaded region implies a higher ORR activity than that on the flat Pt (111) surface. (h) SAs and MAs of different catalysts. This figure has been adapted from ref. 61 with permission from the AAAS, copyright 2016. (i) The configurations of adsorbed intermediates (OOH*, O*, and OH*) on Pd_3Pb (111) slabs for the ORR. (j) The calculated free energy diagrams for the ORR on Pd_3Pb (111) and Pd (111) slabs at the equilibrium potential (U = 1.23 V). (k) The projected density of states for Pd_3Pb (111) and Pd (111) slabs. (l) MAs and SAs at 0.85 and 0.9 V *vs.* RHE for Pd_3Pb UPIN/C, Pd NS/C, Pt/C, and Pd/C. This figure has been adapted from ref. 77 with permission from John Wiley and Sons, copyright 2021. (m) Surface valence band photoemission spectra of Pd_3Pb/Pd NS/C, Pd_3Pb/Pd NC/C, Pd_3Pb NS/C, Pd_3Pb NC/C, and Pd/C. (n) The Gibbs free energy evolution along $4e^-$ reaction processes without considering the effect of pH. (o) MAs and SAs of Pd_3Pb/Pd NS/C, Pd_3Pb/Pd NC/C, Pd_3Pb NS/C, Pd_3Pb NC/C, Pt/C and Pd/C. This figure has been adapted from ref. 69 with permission from the American Chemical Society, copyright 2019.

surface as a function of strain in the [001] and [110] directions were obtained under biaxial strain. Three types of the most stable oxygen adsorption sites on the (110) surface, namely, the *fcc* hollow sites ("h"), the bridge sites in the [001] direction ("b1"), and the bridge sites in the [110] direction ("b2"), were examined, as shown in Fig. 14d, and the calculated ΔE_O results are shown in Fig. 14d–g. The results demonstrated that "h" and "b2" sites exhibited high ORR activity and stability under the appropriate large biaxial strains. As shown in Fig. 14h, the MA and SA of PtPb/Pt core/shell IMNP/C are 4.3 A mg_{Pt}^{-1} and 7.8 mA cm^{-2} at 0.9 V *vs.* RHE. In addition, only 7.7% loss of MA was detected after 50 000 potential cycles of ADTs.

Another effective approach is to prepare 2D ultrathin NSs with abundant defects and perforations to expose more active and defect sites to promote the ORR performance. The grain boundaries and surface distortions can provide plenty of defect sites to benefit the catalytic activity.[84–86] Additionally, the abundant perforations can enlarge the active surface area and provide plentiful electroactive sites, which are also favorable for electron transfer and mass transport.[87,88] Therefore, defect- and channel-rich Pd_3Pb UPINs (Fig. 10) were expected to be perfect electrocatalysts to expose more active sites.[77] In addition, it was expected from DFT calculations that the introduction of Pb into Pd (111) would lead to the optimized electronic structure and thus enhance the ORR performance. Fig. 14i shows the theoretical model of adsorbed intermediate (OOH*, O*, and OH*, where * represents a surface site) configurations for the ORR on the Pd_3Pb (111) slab. The Pd (111) slab is also calculated for comparison. The Gibbs free energies of intermediates on the Pd_3Pb (111) and Pd (111) slabs were calculated by DFT. As depicted in Fig. 14j, OH* → H_2O(l) is the rate-limiting step of the ORR owing to the strong binding of OH* on the Pd_3Pb (111) and Pd (111) slabs. However, Pd_3Pb (111) has an overpotential of only 0.59 V, which is much smaller than that of Pd (111) (0.85 V), demonstrating that the introduction of Pb into Pd (111) is expected to show enhanced catalytic activity toward the ORR. In addition, the adsorption properties of intermediates on a catalyst are basically governed by the surface electronic structure according to d-band theory.[83] The behavior of the occupied d orbital projected on the catalyst surface closely correlates with surface chemisorption and local electron transfer. In the context of the chemisorption of molecules to a metal surface, a lower d-band

center (ε_d, with respect to the Fermi level) results in weaker bonding. Fig. 14k shows the calculated ε_d of surface Pd atoms of Pd_3Pb (111) and Pd (111) slabs. A significant downshift of ε_d of the Pd_3Pb (111) slab (−1.62 eV) was observed compared with that of the Pd (111) slab (−1.43 eV), suggesting that the interatomic interaction between Pd and Pb had a great impact on the electronic structure. Lower ε_d results in a weaker OH* binding energy, which thus significantly enhances the ORR activity for Pd_3Pb UPINs. As a result, Pd_3Pb UPIN/C presents the highest MA of 0.59 A mg_{Pd}^{-1} and a SA of 1.8 mA cm^{-2} in comparison with Pd UN/C, Pt/C, and Pd/C, as shown in Fig. 14l. Besides, Pd_3Pb UPIN/C exhibits negligible MA degradation and unnoticeable changes to the structure and chemical states of the components after 10 000 potential cycles of ADTs. More importantly, strong interatomic interactions between Pd and Pb in the atomically ordered intermetallic structure gives Pd_3Pb UPIN/C with a higher maximum power density and excellent long-term durability compared to Pt/C in the fuel cell test.

The Pd_3Pb/Pd core/shell IMNSs with homogeneous tensile strain along {001} on both the top-Pd and edge-Pd surfaces (Fig. 5a–g) exhibit excellent ORR performance.[69] The introduction of the tensile strain effect into Pd_3Pb/Pd core/shell IMNSs weakens the oxygen binding energy to an optimal value, as shown in Fig. 14m. The Gibbs free energy change in Fig. 14n reveals that the Pd_3Pb/Pd core/shell IMNSs have the lowest overpotential for the ORR. As a result, the strained Pd_3Pb/Pd core/shell IMNSs show MA and SA of 0.574 A mg_{Pd}^{-1} and 1.31 mA cm^{-2} at 0.90 V *vs.* RHE, which are 8.8 (6.5) and 9.4 (9.8) times higher than those of commercial Pd/C (Pt/C), as shown in Fig. 14o, respectively. Besides, Pd_3Pb/Pd core/shell IMNS/C has only 8.1% loss after 20 000 cycles of ADTs; this value is much better than that of Pt/C with over 46.6% loss in MA.

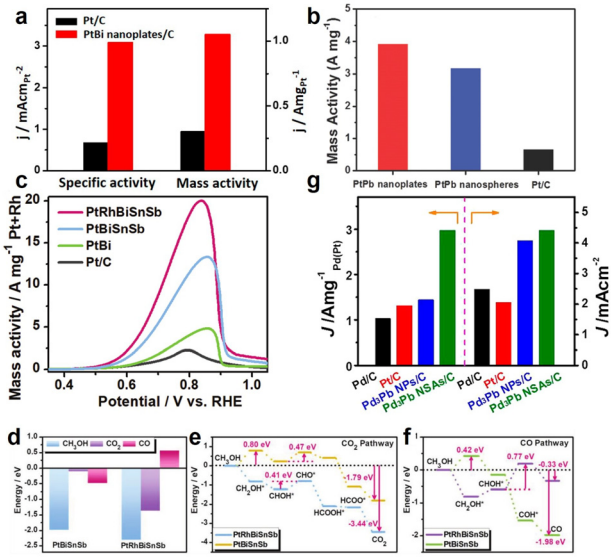

Fig. 15 MOR performances. (a) Histogram of SAs and MAs of PtBi/Pt core/shell IMNP/C and commercial Pt/C in 0.1 M $HClO_4$ solution containing 0.1 M methanol. This figure has been adapted from ref. 57 with permission from the American Chemical Society, copyright 2018. (b) SAs of 2D PtPb IMNPs, PtPb nanospheres, and commercial Pt/C in 1 M KOH containing 1 M methanol. This figure has been adapted from ref. 64 with permission from the Royal Society of Chemistry, copyright 2020. (c) MAs of PtRhBiSnSb, PtBiSnSb IMNPs, PtBi intermetallic catalysts, and commercial Pt/C by recording positive-going polarization curves at a scan rate of 50 mV s^{-1} in 1 M KOH containing 1 M methanol. (d) Adsorption energy comparison of CH_3OH, CO_2, and CO on 2D PtRhBiSnSb high-entropy IMNPs and PtBiSnSb IMNPs. The reaction energy comparison of the CO_2 pathway (e) and CO pathway (f) for the MOR process on 2D PtRhBiSnSb high-entropy IMNPs and PtBiSnSb IMNPs. This figure has been adapted from ref. 67 with permission from John Wiley and Sons, copyright 2022. (g) MAs and SAs of intermetallic Pd_3Pb NSAs, intermetallic Pd_3Pb nanoparticles, Pt/C, and Pd/C in 1 M KOH containing 1 M methanol. This figure has been adapted from ref. 71 with permission from the American Chemical Society, copyright 2018.

4.2. Methanol oxidation reaction

Direct methanol FCs (DMFCs) are promising power sources on account of their large theoretical energy density and high energy conversion efficiency.[47–49] Though the power density of DMFCs is lower than that of PEMFCs fed with hydrogen, liquid methanol fuel is safe and easy to store, transport, and refuel, making DMFCs a perfect candidate for sustainable energy conversion and storage devices for transportable electronic devices.[43,44] However, the high manufacturing cost and poor stability of Pt electrocatalysts lead to poor commercialization. Developing cheap and efficient electrocatalysts for the MOR is the key to boosting the commercialization of DMFCs.[50,51]

The MOR performances of 2D PtBi/Pt core/shell IMNPs (Fig. 2a–d) and commercial Pt/C were evaluated in 0.1 M $HClO_4$ solution containing 0.1 M methanol for comparison.[57] The SA and MA values were obtained by normalizing the peak current to the specific area and mass of Pt, respectively. As shown in Fig. 15a, the SA and MA of 2D PtBi/Pt core/shell IMNP/C reach 3.18 mA cm^{-2} and 1.1 A mg^{-1}, which are 7.4 and 3.7 times higher than those of Pt/C, respectively. In addition, the MOR performances of 2D PtPb IMNPs, PtPb nanospheres, and Pt/C were determined in N_2-saturated 1 M KOH solution containing 1 M methanol, as shown in Fig. 15b. The MA of 2D PtPb IMNPs is 3.9 A mg_{Pt}^{-1}, which is 1.2 times higher than that of PtPb nanospheres (3.16 A mg_{Pt}^{-1}) and 6.1 times higher than that of the Pt/C catalyst (0.64 A mg_{Pt}^{-1}). Additionally, the synergistic effects have a significant influence on the catalytic performance of catalysts.[18,19] Thus, by mixing isolated Pt/Rh/Bi/Sn/Sb atoms, the as-obtained high-entropy 2D PtRhBiSnSb IMNPs achieve a record-high MA of 19.529 A mg^{-1}_{Pt+Rh} towards the MOR, which is 8.6 times higher than that of the Pt/C electrocatalyst, as shown in Fig. 15c.[67] The enhanced MOR performance of high-entropy 2D PtRhBiSnSb IMNPs was compared by calculating the adsorption energy of CH_3OH, CO_2, and CO on high-entropy 2D PtRhBiSnSb IMNPs and PtBiSnSb IMNPs, as shown in Fig. 15d. The adsorption of CH_3OH and CO_2 is strengthened in high-entropy 2D PtRhBiSnSb IMNPs, leading to improved electroactivity toward the oxidation of CH_3OH. Notably, the high-entropy 2D

PtRhBiSnSb IMNPs show an unpreferred adsorption of CO, which supports the stronger resistance toward CO poisoning during the MOR. For the CO_2 pathways, as shown in Fig. 15e, it is noted that the high-entropy 2D PtRhBiSnSb IMNPs deliver a stronger reaction trend with a minor energy barrier of 0.41 eV for CHOH* → CHO* conversion. Moreover, high-entropy 2D PtRhBiSnSb IMNPs have a more negative reaction energy than PtBiSnSb NPs, which further reveals their superior MOR performance. Meanwhile, for the CO pathway, as shown in Fig. 15f, the energy barrier of 0.77 eV for high-entropy 2D PtRhBiSnSb IMNPs is much larger than that for the CO_2 pathway, indicating a stronger selectivity toward CO_2. The MOR performances of fully ordered and highly open Pd_3Pb NSAs (Fig. 5l–n), Pd_3Pb nanoparticles, commercial Pt/C, and Pd/C were evaluated for comparison.[71] Fig. 15g depicts the calculated MAs and SAs by normalizing the peak current in the forward potential scan with regard to the loading amount of Pt or Pd and ECSAs in 1 M KOH containing 1 M methanol solution. Pd_3Pb NSA/C, Pd_3Pb nanoparticle/C, commercial Pt/C, and Pd/C have MAs of 2.98 A mg_{Pd}^{-1}, 1.44 A mg_{Pd}^{-1}, 1.01 A mg_{Pd}^{-1}, 1.31 A mg_{Pt}^{-1}, and SAs of 4.41 mA cm^{-2}, 4.07 mA cm^{-2}, 2.05 mA cm^{-2}, 2.44 mA cm^{-2}, demonstrating the best MOR activity of Pd_3Pb NSAs.

4.3. Ethanol oxidation reaction

Though methanol has significant advantages for use as the fuel supply, unfortunately, methanol is a toxic substance and methanol molecules can cross over the proton exchange membrane to poison the catalysts.[52–55] Ethanol is safer and more economical than methanol.[56] As a result, direct ethanol fuel cells (DEFCs) have attracted much attention for application in portable power devices for vehicles and electronics.[56] In addition to the MOR, the high-entropy 2D PtRhBiSnSb IMNPs also exhibit enhanced EOR performance. As shown in Fig. 16a, the as-obtained 2D PtRhBiSnSb IMNPs achieve the highest MA of 15.558 A mg^{-1}_{Pt+Rh} towards the EOR, which is 10.4 times higher than that of the Pt/C electrocatalyst.[67] In addition, the EOR performances of intermetallic *fct* PdZn NSs (Fig. 6a–e), pure Pd NSs, and Pd black were evaluated for comparison.[74] The cyclic voltammetry (CV) profiles of *fct* PdZn NSs, Pd NSs, and Pd black in Fig. 16b recorded the MAs of *fct* PdZn NSs (2.73 A mg_{Pd}^{-1}), pure Pd NSs (1.57 A mg_{Pd}^{-1}) and Pd black (0.92 A mg_{Pd}^{-1}), demonstrating that the *fct* PdZn NSs had the greatest current density and best activity for the EOR among the three catalysts. Fig. 16c shows the CVs of Pd_8Sb_3 HNP/C, commercial Pd/C, and Pt/C in 0.5 M NaOH containing 0.5 M ethanol with a sweep rate of 50 mV s^{-1}.[76] A lower onset potential and larger current intensity of Pd_8Sb_3 HNP/C were observed in comparison with commercial Pd/C and Pt/C, suggesting better anodic electrooxidation activity. Pd_8Sb_3 HNP/C shows the highest SA of 29.3 mA cm^{-2} and MA of 4.5 A mg_{Pd}^{-1}. The SA of Pd_8Sb_3 HNP/C is 7.0 and 9.8 times higher than those of commercial Pd/C (4.2 mA cm^{-2}) and Pt/C (3.0 mA cm^{-2}). Meanwhile, the MA of Pd_8Sb_3 HNP/C is 11.3 and 3.8 times higher than those of Pd/C (0.4 A mg_{Pd}^{-1}) and Pt/C (1.2 A mg_{Pt}^{-1}). Fig. 16d shows the calculated EOR thermodynamic energy change diagrams for the Pd_8Sb_3 (001) and Pd (111) planes. The potential determining step (PDS) for the EOR on the Pd_8Sb_3 (001) plane is the dehydrogenation of CH_3CH_2OH* to CH_3CH_2O* with an energy input of 0.99 eV, which is lower than that for Pd (111) (1.08 eV). In addition, the desorption energy of CH_3COOH* from CH_3COOH on Pd_8Sb_3 is −0.67 eV, which is more positive than that on Pd (111) (−0.83 eV). All the evidence indicates that the Pd_8Sb_3 HNPs exhibit a higher EOR activity than that of Pd.

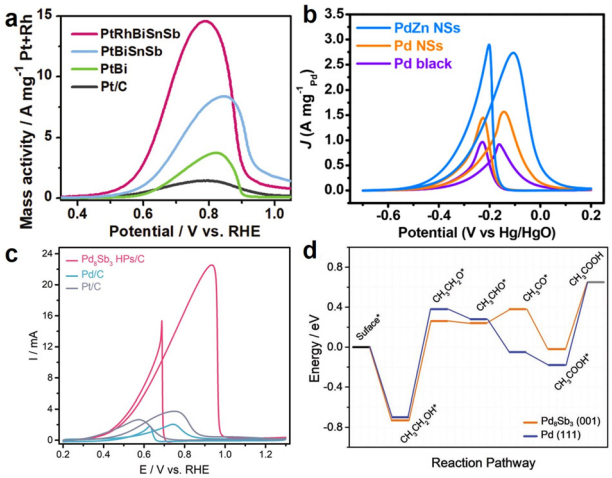

Fig. 16 EOR performances. (a) Positive-going polarization curves of PtRhBiSnSb IMNP/C, PtBiSnSb IMNP/C, PtBi IMNP/C, and commercial Pt/C in 1.0 M KOH + 1.0 M C_2H_5OH solution recorded at a scan rate of 50 mV s^{-1}. This figure has been adapted from ref. 67 with permission from John Wiley and Sons, copyright 2022. (b) CV profiles of PdZn IMNSs, Pd NSs, and Pd black measured in a mixture of 1.0 M NaOH and 1.0 M ethanol at scan rate of 50 mV s^{-1}. This figure has been adapted from ref. 74 with permission from the American Chemical Society, copyright 2019. (c) CVs of Pd_8Sb_3 HNPs /C, commercial Pd/C, and Pt/C in 0.5 M NaOH containing 0.5 M ethanol with a sweep rate of 50 mV s^{-1}. (d) The energy changes ΔE (eV) of Pd_8Sb_3 (001) and Pd (111) planes throughout the EOR. This figure has been adapted from ref. 76 with permission from John Wiley and Sons, copyright 2022.

4.4. Formic acid oxidation reaction

Formic acid exhibits lower toxicity and fuel crossover rates through Nafion membranes than other commonly used fuels like methanol, which make it a potential candidate fuel.[45,46] The FAOR performances of PtBi@0.9% Pd IMNPs, PtBi@1.8% Pd IMNPs, PtBi@3.0%Pd IMNPs, PtBi IMNPs, Pt/C, and Pd black catalysts were evaluated by recording the anode polarization curves of forward linear sweep voltammograms from 0.3 to 0.8 V *vs.* a saturated calomel electrode (SCE) in Ar-saturated 0.5 M H_2SO_4 + 1.0 M HCOOH solution.[79] As shown in Fig. 17a, the PtBi@1.8%Pd IMNPs achieved the highest MA of 4.17 A mg^{-1}_{Pt+Pd}, which was 27, 9.6, and 3.8 times higher than those of commercial Pt/C (0.16 A mg^{-1}), Pd black (0.43 A mg^{-1}), and PtBi HNPs (1.09 A mg^{-1}), respectively. Additionally, Fig. 17a illustrates the volcano trends of MAs plotted as a function of the binding energy (Pt $4f_{7/2}$) of PtBi@0.9% Pd, PtBi@1.8%Pd, and PtBi@3.0%Pd IMNPs, in which PtBi@1.8%Pd IMNPs have

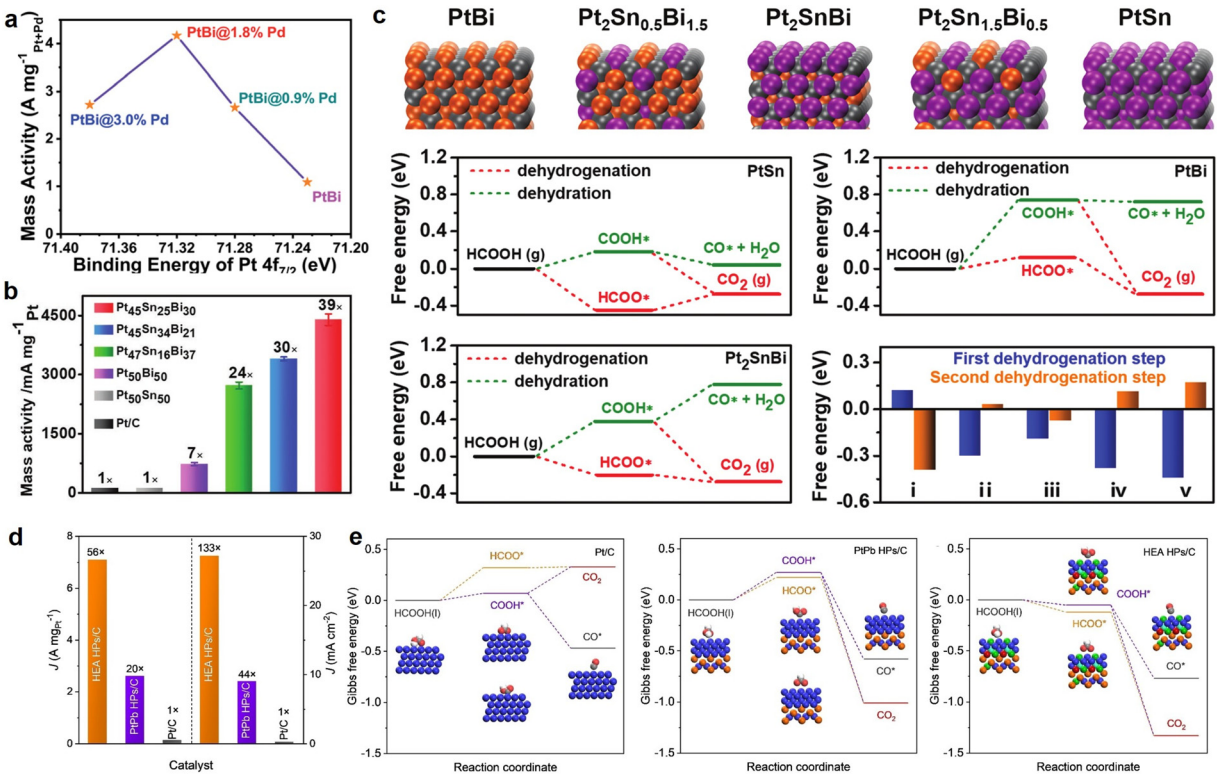

Fig. 17 FAOR performances. (a) Volcano trends of FAOR activities plotted as a function of the binding energies of Pt $4f_{7/2}$ of PtBi@0.9%Pd, PtBi@1.8%Pd, and PtBi@3.0%Pd IMNPs. This figure has been adapted from ref. 79 with permission from the Royal Society of Chemistry, copyright 2021. (b) The MAs of $Pt_{45}Sn_{25}Bi_{30}$, $Pt_{45}Sn_{34}Bi_{21}$, $Pt_{47}Sn_{16}Bi_{37}$, $Pt_{50}Bi_{50}$, and $Pt_{50}Sn_{50}$. (c) DFT calculation of the FAOR on different PtSnBi NPs including dehydrogenation and dehydration pathways. This figure has been adapted from ref. 65 with permission from John Wiley and Sons, copyright 2019. (d) MAs and SAs and (e) the Gibbs free energy diagrams of high-entropy 2D PtBiPbNiCo HNP/C, PtPb HNPd/C, and Pt/C for the FAOR. This figure has been adapted from ref. 68 with permission from John Wiley and Sons, copyright 2023.

the highest MA at an appropriate binding energy (Pt $4f_{7/2}$) of 71.32 eV. Thus, introducing appropriate Pd atoms results in a suitable binding energy of Pt 4f, contributed to by effective Bi (downward shift) and Pd (upward shift) modification, that benefits the FAOR electrocatalysis compared with Pt/C and PtBi. In addition, 2D PtSnBi IMNPs with controllable compositions ($Pt_{47}Sn_{16}Bi_{37}$, $Pt_{45}Sn_{25}Bi_{30}$, and $Pt_{45}Sn_{34}Bi_{21}$), $Pt_{50}Bi_{50}$ IMNPs, and $Pt_{50}Sn_{50}$ IMNPs were evaluated and benchmarked against commercial Pt/C.[65] Typical FAOR anodic scan polarization curves of forward linear sweep voltammograms from −0.2 to 0.8 V *vs.* SCE in Ar-saturated 0.5 M H_2SO_4 + 1.0 M HCOOH solution were recorded. A volcano plot for the composition-dependent FAOR activity of PtSnBi IMNPs is demonstrated by the order of $Pt_{45}Sn_{25}Bi_{30}$ > $Pt_{45}Sn_{34}Bi_{21}$ > $Pt_{47}Sn_{16}Bi_{37}$ > $Pt_{50}Bi_{50}$ > $Pt_{50}Sn_{50}$, as shown in Fig. 17b. $Pt_{45}Sn_{25}Bi_{30}$, $Pt_{45}Sn_{34}Bi_{21}$, and $Pt_{47}Sn_{16}Bi_{37}$ IMNPs exhibit super high averaged mass activities of 4.394, 3.397, and 2.718 A mg_{Pt}^{-1}, which are about 39/30/24 times and 6/5/4 times higher than that of $Pt_{50}Sn_{50}$ (also commercial Pt/C) and $Pt_{50}Bi_{50}$ IMNPs, respectively. These results demonstrate the great improvement of the ternary PtSnBi composition over the binary composition in boosting the FAOR, indicating the synergism of Pt/Sn/Bi metals. Sn can react with H_2O to form $Sn–OH_{ads}$ at low overpotential, while the high FAOR activity comes from the enhanced selectivity of the direct oxidation of HCOOH. Furthermore, DFT calculations (Fig. 17c) revealed that the FAOR activity originated mainly from the optimized direct oxidation pathway through two dehydrogenation steps (HCOOH to HCOO* and HCOO* to CO_2) and the inhibition of the dehydration path. Fig. 17d shows the MAs and SAs of high-entropy 2D PtBiPbNiCo HNP/C, PtPb HNP/C, and Pt/C for the FAOR.[68] The high-entropy 2D PtBiPbNiCo HNP/C exhibits the highest MA (7.1 A mg_{Pt}^{-1}) and SA (27.2 mA cm^{-2}), which are 3 and 56 times larger than those of PtPb HNP/C (2.6 A mg_{Pt}^{-1}) and commercial Pt/C (0.127 A mg_{Pt}^{-1}) in MA, 3 and 133 times higher than those of PtPb HNP/C (9.0 mA cm^{-2}) and commercial Pt/C (0.205 mA cm^{-2}) in SA, respectively. DFT calculations were carried out to compare the thermochemical reaction energetics of the FAOR *via* dehydrogenation and dehydration pathways on PtBiPbNiCo HNP/C, PtPb HNP/C, and Pt/C substrates. Fig. 17e shows the corresponding intermediates (HCOO*, COOH* and CO*) and free energy profiles. The Gibbs free energy diagram of Pt/C indicates that the dehydration pathway is energetically favorable due to the stronger binding of CO* on the surface than CO_2, leading to low FAOR activity. Furthermore, the first dehydrogenation step is the rate-determining step for PtPb HNP/C, whereas no rate-determining step exists on PtBiPbNiCo HNP/C due to both dehydrogenation

steps (HCOOH to HCOO* and COOH*) being exothermic reactions. The two dehydrogenation steps are downhill (0.05 and 0.12 eV) on the PtBiPbNiCo HNP/C surface, implying a facile reaction for the two dehydrogenation steps and superior FAOR performance. By forming PtBiPbNiCo HNPs, the dehydrogenation steps are optimized compared with that of PtPb HNPs, indicating that enriched Bi in the shell promotes HCOO* and COOH* adsorption by Pt. Hence, the high activity of PtBiPbNiCo HNPs for the FAOR can be attributed to the suppression of the dehydration path and optimization of the two dehydrogenation steps.

5. Summary and perspectives

The 2D Pt- and Pd-based IMNPs and IMNSs exhibit enhanced catalytic activity and robust durability for several FC-related reactions including the ORR, MOR, EOR, and FAOR. In this review, we summarized the syntheses of Pt- and Pd-based IMNPs and IMNSs by one-pot synthesis, seed-mediated synthesis, and the combination of these two methods. The unique structures with large surface areas, optimized adsorption energy of intermediates, strong interaction between metal atoms, and ordered arrangement of atoms of Pt- and Pd-based IMNPs and IMNSs achieved enhanced catalytic activity and durability toward the ORR, MOR, EOR, and FAOR. Therefore, Pt- and Pd-based IMNPs and IMNSs have gained increasing interest as potential candidates for application in FCs. However, there are still many challenges in terms of preparing well-controlled Pt- and Pd-based IMNPs and IMNSs with higher activity, better stability, and lower cost.

5.1 Seed-mediated synthesis of 2D Pt-based IMNPs and IMNSs

Seed-mediated synthesis is a powerful strategy to prepare IMNCs with well-controlled dispersity, size, and composition.[89,90] For example, 2D Pd–Pb, Pd–Sn, and Pd–Cd IMNSs with abundant pores,[77] rich channels and grain boundaries[78] were prepared using the seed-mediated synthesis method. However, such perforated Pt-based nanostructures, which have high specific surface active areas with abundant active sites to improve the electrocatalytic activity and promote electron transport and mass transfer, are rarely reported. Therefore, the seed-mediated synthesis of perforated Pt-based IMNPs and IMNSs is highly desirable for introducing metal elements with relatively large thermal diffusion coefficients (Ni, Sn) into Pt NPs and NSs.[90]

5.2 Improving the intrinsic activity of the 2D Pt- and Pd-based IMNPs and IMNSs

Two main factors strongly affect the electrocatalytic performance of an electrocatalyst: the intrinsic activity of each active site and the number of exposed active sites. Improving the intrinsic activity of each active site is effective at enhancing the overall performance of a catalyst. The exposed crystal facet significantly affects the catalytic performance. For example, the Pd_3Pb SNP with {100} orientation shows a higher ORR catalytic activity than that of Pd_3Pb NPAs with {111} facets.[70] Synthesizing multimetallic metals offers additional flexibility in terms of optimizing their catalytic properties toward a specific reaction.[65–68] Surface strain can modulate the surface electronic structure and alter the interactions between intermediate species and active sites.[81,82] Therefore, constructing Pt- and Pd-based IMNPs and IMNSs featuring favorable active facets, a strong synergistic effect with alloying elements, and a modulated electronic structure with appropriate strain engineering is still a significant challenge but extremely effective at enhancing the electrocatalytic performance.

5.3 Exposing more active sites of the 2D Pt- and Pd-based IMNPs and IMNSs

The number of exposed active sites directly affects the electrocatalytic performance of catalysts. An effective strategy is to prepare Pt- and Pd-based IMNPs and IMNSs with abundant grain boundaries, surface distortions, and perforations to expose more active sites. However, the usage of appropriate surfactants (*e.g.*, CTAB, PVP) is inevitable during the preparation process by wet-chemistry synthesis. Surfactants attached to the surface of Pt- and Pd-based IMNPs and IMNSs cover a large number of surface active sites and inhibit the electrocatalytic performance. The surfactants attached to the surfaces can be effectively removed by plasma cleaning,[91] acid,[92] and UV–ozone treatments.[93] In addition, Zheng and co-workers prepared surface-clean uniform Pd NSs by simply mixing $[Pd_2(\mu\text{-}CO)_2Cl_4]^{2-}$ with H_2O.[94] Therefore, constructing Pt- and Pd-based IMNPs and IMNSs in the absence of any organic capping agent or with thorough removal of the surfactant are effective approaches for exposing more active sites and enhancing the electrocatalytic performance.

5.4 Lowering the cost for preparing the 2D Pt- and Pd-based IMNPs and IMNSs

The cost of catalysts is important for practical applications. Therefore, to lower the cost of Pt- and Pd-based IMNPs and IMNSs for industrial applications, greater partial replacement of Pt and Pd with non-noble metals and a comparable electrocatalytic performance is critical. For instance, PtFe with a lower Pt content is more economical compared with Pt_3Fe. As a result, one effective strategy for reducing the cost is to construct Pt- and Pd-based IMNPs and IMNSs with low contents of Pt and Pd.

5.5 Enhancing the stability of the 2D Pt- and Pd-based IMNPs and IMNSs during electrochemical reactions

Better stability can also reduce the maintenance cost of catalysts for practical applications. However, the inevitable leaching of non-noble metals and aggregation of nanoparticles during the electrocatalytic reaction destroys the original structure, leading to weakened stability. It was reported that nitrogen doping prevented the dissolution of the transition metal cobalt of the N-doped Pt_3Co intermetallic nanocatalyst (Pt_3CoN/C), which gave Pt_3CoN/C superior ORR activity and

durability compared to undoped Pt_3Co/C.[95] In addition, Wang and colleagues developed an N-doped carbon layer encapsulating Pd–Fe intermetallic nanoparticles, which exhibited outstanding stability with only 2 mV $E_{1/2}$ decay after 30 000 potential cycles even in O_2-saturated $HClO_4$.[96] Thus, one effective strategy is to protect the Pt- and Pd-based IMNPs and IMNSs by doping or confining the catalysts with a coating layer. Yet more strategies need to be developed.

5.6 Toward the large-scale practical production of the 2D Pt- and Pd-based IMNPs and IMNSs

Until now, it was difficult to produce 2D Pt- and Pd-based IMNPs and IMNSs with rationally designed structures at commercial scales to enable the future industrialization of FCs. Most of the current prepared 2D Pt- and Pd-based IMNPs and IMNSs were evaluated under laboratory conditions. However, it is difficult to ensure their activity and stability when applied to large-scale practical production.

Taken together, Pt- and Pd-based IMNPs and IMNSs show great potential for FCs but face many new challenges. We believe that these blossoming catalysts will reach greater achievements and hope this review can provide guidelines for future explorations and new applications of Pt- and Pd-based IMNPs and IMNSs.

Author contributions

Jingchun Guo: conceptualization, writing original draft, review and editing. Wei Liu, Xucheng Fu and Shilong Jiao: review and editing. All authors contributed to the discussion and commented on the article.

Conflicts of interest

There are no conflicts to declare.

Acknowledgements

This research was supported by the Natural Science Research of Universities in Anhui (KJ2020A0629, 2022AH051685), the Provincial Quality Engineering Project of Anhui Provincial Education Department (2021xsxxkc326), high-level talent research start-up fee funding from West Anhui University (WGKQ2021033, WGKQ2022043), the Key Research and Development Projects in Anhui Province (202004b11020021), the 8th Special Support Plan Innovative Talents Project of Anhui Province (FU), the China Postdoctoral Science Foundation under Grant No. 2021M701065, and the Key Research & Development and Promotion Project of Henan Province (Science and Technology Tackling Key Problems, 222102240070).

References

1 J. Lelieveld, K. Klingmuller, A. Pozzer, R. T. Burnett, A. Haines and V. Ramanathan, *Proc. Natl. Acad. Sci. U. S. A.*, 2019, **116**, 7192–7197.
2 S. C. Peter, *ACS Energy Lett.*, 2018, **3**, 1557–1561.
3 F. Martins, C. Felgueiras, M. Smitkova and N. Caetano, *Energies*, 2019, **12**, 964.
4 J. Y. Kim, J. W. Lee, H. S. Jung, H. Shin and N. G. Park, *Chem. Rev.*, 2020, **120**, 7867–7918.
5 M. Riede, D. Spoltore and K. Leo, *Adv. Energy Mater.*, 2021, **11**, 2002653.
6 E. Fan, L. Li, Z. Wang, J. Lin, Y. Huang, Y. Yao, R. Chen and F. Wu, *Chem. Rev.*, 2020, **120**, 7020–7063.
7 Y. Tian, G. Zeng, A. Rutt, T. Shi, H. Kim, J. Wang, J. Koettgen, Y. Sun, B. Ouyang, T. Chen, Z. Lun, Z. Rong, K. Persson and G. Ceder, *Chem. Rev.*, 2021, **121**, 1623–1669.
8 F. Xiao, Y. C. Wang, Z. P. Wu, G. Chen, F. Yang, S. Zhu, K. Siddharth, Z. Kong, A. Lu, J. C. Li, C. J. Zhong, Z. Y. Zhou and M. Shao, *Adv. Mater.*, 2021, **33**, e2006292.
9 S. Zaman, L. Huang, A. I. Douka, H. Yang, B. You and B. Y. Xia, *Angew. Chem., Int. Ed.*, 2021, **60**, 17832–17852.
10 X. Wang, Z. Li, Y. Qu, T. Yuan, W. Wang, Y. Wu and Y. Li, *Chem*, 2019, **5**, 1486–1511.
11 C. Wan, X. Duan and Y. Huang, *Adv. Energy Mater.*, 2020, **10**, 1903815.
12 X. Tian, X. F. Lu, B. Y. Xia and X. W. Lou, *Joule*, 2020, **4**, 45–68.
13 J. Zhang, Y. Yuan, L. Gao, G. Zeng, M. Li and H. Huang, *Adv. Mater.*, 2021, **33**, e2006494.
14 W. Li, D. Wang, Y. Zhang, L. Tao, T. Wang, Y. Zou, Y. Wang, R. Chen and S. Wang, *Adv. Mater.*, 2020, **32**, e1907879.
15 M. Zhou, C. Li and J. Fang, *Chem. Rev.*, 2021, **121**, 736–795.
16 Y. Yan, J. S. Du, K. D. Gilroy, D. Yang, Y. Xia and H. Zhang, *Adv. Mater.*, 2017, **29**, 1605997.
17 E. Antolini, *Appl. Catal., B*, 2017, **217**, 201–213.
18 W. Xiao, W. Lei, M. Gong, H. L. Xin and D. Wang, *ACS Catal.*, 2018, **8**, 3237–3256.
19 H. Sun, S. Song, X. Xu, J. Dai, J. Yu, W. Zhou, Z. Shao and W. Jung, *Adv. Energy Mater.*, 2021, **11**, 2101937.
20 C. Cui, H. Li, X. Liu, M. Gao and S. Yu, *ACS Catal.*, 2012, **2**, 916–924.
21 D. Chung, S. Jun, G. Yoon, S. Kwon, D. Shin, P. Seo, J. Yoo, H. Shin, Y. Chung, H. Kim, B. Mun, K. Lee, N. Lee, S. Yoo, D. Lim, K. Kang, Y. Sung and T. Hyeon, *J. Am. Chem. Soc.*, 2015, **137**, 15478–15485.
22 Y. Yuan, Z. Yang, W. Lai, L. Gao, M. Li, J. Zhang and H. Huang, *Chem. – Eur. J.*, 2021, **27**, 16564–16580.
23 W. Wang, F. Lv, B. Lei, S. Wan, M. Luo and S. Guo, *Adv. Mater.*, 2016, **28**, 10117–10141.
24 Q. Shao, K. Lu and X. Huang, *Small Methods*, 2019, **3**, 1800545.
25 H. Xu, H. Shang, C. Wang and Y. Du, *Adv. Funct. Mater.*, 2020, **30**, 2000793.
26 Y. Wang, Y. Yuan and H. Huang, *Chin. J. Chem.*, 2021, **39**, 1389–1396.

27 M. A. Zeb Gul Sial, M. A. Ud Din and X. Wang, *Chem. Soc. Rev.*, 2018, **47**, 6175–6200.
28 H. Jin, C. Guo, X. Liu, J. Liu, A. Vasileff, Y. Jiao, Y. Zheng and S. Z. Qiao, *Chem. Rev.*, 2018, **118**, 6337–6408.
29 Y. Chen, Z. Fan, Z. Zhang, W. Niu, C. Li, N. Yang, B. Chen and H. Zhang, *Chem. Rev.*, 2018, **118**, 6409–6455.
30 M. Luo, Y. Yang, Y. Sun, Y. Qin, C. Li, Y. Li, M. Li, S. Zhang, D. Su and S. Guo, *Mater. Today*, 2019, **23**, 45–56.
31 F. Nosheen, N. Wasfi, S. Aslam, T. Anwar, S. Hussain, N. Hussain, S. N. Shah, N. Shaheen, A. Ashraf, Y. Zhu, H. Wang, J. Ma, Z. Zhang and W. Hu, *Nanoscale*, 2020, **12**, 4219–4237.
32 S. Chen, Z. Niu, C. Xie, M. Gao, M. Lai, M. Li and P. Yang, *ACS Nano*, 2018, **12**, 8697–8705.
33 J. Park, T. Kwon, J. Kim, H. Jin, H. Y. Kim, B. Kim, S. H. Joo and K. Lee, *Chem. Soc. Rev.*, 2018, **47**, 8173–8202.
34 L. Ji, J. Wang, X. Teng, T. J. Meyer and Z. Chen, *ACS Catal.*, 2020, **10**, 412–419.
35 H. Y. Kim, T. Kwon, Y. Ha, M. Jun, H. Baik, H. Y. Jeong, H. Kim, K. Lee and S. H. Joo, *Nano Lett.*, 2020, **20**, 7413–7421.
36 T. H. Yang, J. Ahn, S. Shi, P. Wang, R. Gao and D. Qin, *Chem. Rev.*, 2021, **121**, 796–833.
37 M. Luo, Z. Zhao, Y. Zhang, Y. Sun, Y. Xing, F. Lv, Y. Yang, X. Zhang, S. Hwang, Y. Qin, J. Y. Ma, F. Lin, D. Su, G. Lu and S. Guo, *Nature*, 2019, **574**, 81–85.
38 L. Tang, X. Meng, D. Deng and X. Bao, *Adv. Mater.*, 2019, **31**, e1901996.
39 H. Xu, H. Shang, C. Wang and Y. Du, *Small*, 2021, **17**, e2005092.
40 J. Guo, S. Jiao, X. Ya, H. Zheng, R. Wang, J. Yu, H. Wang, Z. Zhang, W. Liu, C. He and X. Fu, *ChemElectroChem*, 2022, **9**, e202200729.
41 B. Xu, Y. Zhang, L. Li, Q. Shao and X. Huang, *Coord. Chem. Rev.*, 2022, **459**, 214388.
42 M. Zhou, J. Guo and J. Fang, *Small Struct.*, 2022, **3**, 2100188.
43 L. Gong, Z. Yang, K. Li, W. Xing, C. Liu and J. Ge, *J. Energy Chem.*, 2018, **27**, 1618–1628.
44 Z. Xia, X. Zhang, H. Sun, S. Wang and G. Sun, *Nano Energy*, 2019, **65**, 104048.
45 A. Han, Z. Zhang, J. Yang, D. Wang and Y. Li, *Small*, 2021, **17**, e2004500.
46 T. Yang, S. Hou, J. Xing, C. Liu, J. Ge and W. Xing, *Nano Res.*, 2023, **16**, 3607–3621.
47 J. Sheng, J. Kang, H. Ye, J. Xie, B. Zhao, X.-Z. Fu, Y. Yu, R. Sun and C.-P. Wong, *J. Mater. Chem. A*, 2018, **6**, 3906–3912.
48 J. Li, Z. Luo, Y. Zuo, J. Liu, T. Zhang, P. Tang, J. Arbiol, J. Llorca and A. Cabot, *Appl. Catal., B*, 2018, **234**, 10–18.
49 E. Antolini, *Appl. Catal., B*, 2018, **237**, 491–503.
50 M. Mansor, S. N. Timmiati, K. L. Lim, W. Y. Wong, S. K. Kamarudin and N. H. Nazirah Kamarudin, *Int. J. Hydrogen Energy*, 2019, **44**, 14744–14769.
51 A. Ali and P. K. Shen, *J. Mater. Chem. A*, 2019, **7**, 22189–22217.
52 J. Bai, D. Liu, J. Yang and Y. Chen, *ChemSusChem*, 2019, **12**, 2117–2132.
53 R. Rizo, S. Pérez-Rodríguez and G. García, *ChemElectroChem*, 2019, **6**, 4725–4738.
54 Y. Zheng, X. Wan, X. Cheng, K. Cheng, Z. Dai and Z. Liu, *Catalysts*, 2020, **10**, 166.
55 F. Lyu, M. Cao, A. Mahsud and Q. Zhang, *J. Mater. Chem. A*, 2020, **8**, 15445–15457.
56 L. Yaqoob, T. Noor and N. Iqbal, *RSC Adv.*, 2021, **11**, 16768–16804.
57 Y. Qin, M. Luo, Y. Sun, C. Li, B. Huang, Y. Yang, Y. Li, L. Wang and S. Guo, *ACS Catal.*, 2018, **8**, 5581–5590.
58 Y. Feng, Q. Shao, F. Lv, L. Bu, J. Guo, S. Guo and X. Huang, *Adv. Sci.*, 2020, **7**, 1800178.
59 X. Li, Y. Sun, C. Shen, Z. Zheng, H. Chen, Y. Jiang and Z. Xie, *ACS Appl. Energy Mater.*, 2021, **4**, 9190–9197.
60 C. Y. Wang, Z. Y. Yu, G. Li, Q. T. Song, G. Li, C. X. Luo, S. H. Yin, B. A. Lu, C. Xiao, B. B. Xu, Z. Y. Zhou, N. Tian and S. G. Sun, *ChemElectroChem*, 2020, **7**, 239–245.
61 L. Bu, N. Zhang, S. Guo, X. Zhang, J. Li, J. Yao, T. Wu, G. Lu, J. Y. Ma, D. Su and X. Huang, *Science*, 2016, **354**, 1410–1414.
62 Y. Sun, Y. Liang, M. Luo, F. Lv, Y. Qin, L. Wang, C. Xu, E. Fu and S. Guo, *Small*, 2018, **14**, 1702259.
63 Y. Liang, Y. Sun, X. Wang, E. Fu, J. Zhang, J. Du, X. Wen and S. Guo, *Nanoscale*, 2018, **10**, 11357–11364.
64 L. Chen, L. Zhou, H. Lu, Y. Zhou, J. Huang, J. Wang, Y. Wang, X. Yuan and Y. Yao, *Chem. Commun.*, 2020, **56**, 9138–9141.
65 S. Luo, W. Chen, Y. Cheng, X. Song, Q. Wu, L. Li, X. Wu, T. Wu, M. Li, Q. Yang, K. Deng and Z. Quan, *Adv. Mater.*, 2019, **31**, e1903683.
66 Z. Zhu, F. Liu, J. Fan, Q. Li, Y. Min and Q. Xu, *ACS Appl. Mater. Interfaces*, 2020, **12**, 52731–52740.
67 W. Chen, S. Luo, M. Sun, X. Wu, Y. Zhou, Y. Liao, M. Tang, X. Fan, B. Huang and Z. Quan, *Adv. Mater.*, 2022, **34**, e2206276.
68 C. Zhan, L. Bu, H. Sun, X. Huang, Z. Zhu, T. Yang, H. Ma, L. Li, Y. Wang, H. Geng, W. Wang, H. Zhu, C. W. Pao, Q. Shao, Z. Yang, W. Liu, Z. Xie and X. Huang, *Angew. Chem., Int. Ed.*, 2023, **62**, e202213783.
69 C. Tang, N. Zhang, Y. Ji, Q. Shao, Y. Li, X. Xiao and X. Huang, *Nano Lett.*, 2019, **19**, 1336–1342.
70 K. Wang, Y. Qin, F. Lv, M. Li, Q. Liu, F. Lin, J. Feng, C. Yang, P. Gao and S. Guo, *Small Methods*, 2018, **2**, 1700331.
71 L. Bu, C. Tang, Q. Shao, X. Zhu and X. Huang, *ACS Catal.*, 2018, **8**, 4569–4575.
72 S. Luo, M. Tang, X. Wu, Y. Ou, Z. Wang, N. Jian, X. Li, Y. Lin, Y. Yan, J. Huang, H. Zhang and D. Yang, *CrystEngComm*, 2019, **21**, 290–296.
73 S. Luo, Y. Ou, L. Li, J. Li, X. Wu, Y. Jiang, M. Gao, X. Yang, H. Zhang and D. Yang, *Nanoscale*, 2019, **11**, 17301–17307.
74 Q. Yun, Q. Lu, C. Li, B. Chen, Q. Zhang, Q. He, Z. Hu, Z. Zhang, Y. Ge, N. Yang, J. Ge, Y. B. He, L. Gu and H. Zhang, *ACS Nano*, 2019, **13**, 14329–14336.

75 J. Liang, Y. Xia, X. Liu, F. Huang, J. Liu, S. Li, T. Wang, S. Jiao, R. Cao, J. Han, H. L. Wang and Q. Li, *SusMat*, 2022, **2**, 347–356.
76 Y. Zhang, X. Liu, T. Liu, X. Ma, Y. Feng, B. Xu, W. Cai, Y. Li, D. Su, Q. Shao and X. Huang, *Adv. Mater.*, 2022, **34**, e2202333.
77 J. Guo, L. Gao, X. Tan, Y. Yuan, J. Kim, Y. Wang, H. Wang, Y. J. Zeng, S. I. Choi, S. C. Smith and H. Huang, *Angew. Chem., Int. Ed.*, 2021, **60**, 10942–10949.
78 J. Liang, S. Li, Y. Chen, X. Liu, T. Wang, J. Han, S. Jiao, R. Cao and Q. Li, *J. Mater. Chem. A*, 2020, **8**, 15665–15669.
79 M. Tang, W. Chen, S. Luo, X. Wu, X. Fan, Y. Liao, X. Song, Y. Cheng, L. Li, L. Tan, Y. Liu and Z. Quan, *J. Mater. Chem. A*, 2021, **9**, 9602–9608.
80 W. Chen, S. Luo, M. Sun, M. Tang, X. Fan, Y. Cheng, X. Wu, Y. Liao, B. Huang and Z. Quan, *Small*, 2022, **18**, e2107803.
81 M. Li, Z. Zhao, T. Cheng, A. Fortunelli, C.-Y. Chen, R. Yu, Q. Zhang, L. Gu, B. V. Merinov, Z. Lin, E. Zhu, T. Yu, Q. Jia, J. Guo, L. Zhang, W. A. Goddard III, Y. Huang and X. Duan, *Science*, 2016, **354**, 1414–1419.
82 Q. Xu, W. Chen, Y. Yan, Z. Wu, Y. Jiang, J. Li, T. Bian, H. Zhang, J. Wu and D. Yang, *Sci. Bull.*, 2018, **63**, 494–501.
83 J. Nørskov, J. Rossmeisl, A. Logadottir, L. Lindqvist, J. Kitchin, T. Bligaard and H. Jlnsson, *J. Phys. Chem. B*, 2004, **108**, 17886–17892.
84 J. Guo, H. Wang, F. Xue, D. Yu, L. Zhang, S. Jiao, Y. Liu, Y. Lu, M. Liu, S. Ruan, Y.-J. Zeng, C. Ma and H. Huang, *J. Mater. Chem. A*, 2019, **7**, 20247–20253.
85 S. Liu, J. Xiao, X. F. Lu, J. Wang, X. Wang and X. W. D. Lou, *Angew. Chem., Int. Ed.*, 2019, **58**, 8499–8503.
86 M. Li, Y. Yuan, Z. Yao, L. Gao, J. Zhang and H. Huang, *Chem. – Asian J.*, 2020, **15**, 3254–3265.
87 L. Y. Zhang, Y. Ouyang, S. Wang, D. Wu, M. Jiang, F. Wang, W. Yuan and C. M. Li, *Small*, 2019, **15**, e1904245.
88 H. Yu, T. Zhou, Z. Wang, Y. Xu, X. Li, L. Wang and H. Wang, *Angew. Chem., Int. Ed.*, 2021, **60**, 12027–12031.
89 Y. Xia, K. D. Gilroy, H. C. Peng and X. Xia, *Angew. Chem., Int. Ed.*, 2017, **56**, 60–95.
90 J. Guo, S. Jiao, X. Ya, H. Zheng, R. Wang, J. Yu, H. Wang, Z. Zhang, W. Liu, C. He and X. Fu, *Chem. – Eur. J.*, 2022, **28**, e202202221.
91 B. Gehl, A. Frçmsdorf, V. Aleksandrovic, T. Schmidt, A. Pretorius, J. I. Flege, S. Bernstorff, A. Rosenauer, J. Falta and H. Weller, *Adv. Funct. Mater.*, 2008, **18**, 2398–2410.
92 V. Mazumder and S. Sun, *J. Am. Chem. Soc.*, 2009, **131**, 4588.
93 M. Crespo-Quesada, J.-M. Andanson, A. Yarulin, B. Lim, Y. Xia and L. Kiwi-Minsker, *Langmuir*, 2011, **27**, 7909–7916.
94 H. Li, G. Chen, H. Yang, X. Wang, J. Liang, P. Liu, M. Chen and N. Zheng, *Angew. Chem.*, 2013, **125**, 8526–8530.
95 M. Liu, A. Hu, Y. Ma, G. Wang, L. Zou, X. Chen and H. Yang, *J. Electroanal. Chem.*, 2020, **871**, 114267.
96 Y. Hu, Y. Lu, X. Zhao, T. Shen, T. Zhao, M. Gong, K. Chen, C. Lai, J. Zhang, H. L. Xin and D. Wang, *Nano Res.*, 2020, **13**, 2365–2370.